A multidimensional analysis reveals distinct immune phenotypes and tertiary lymphoid structure-like aggregates in the bone marrow of pediatric acute myeloid leukemia

Joost B. Koedijk[1,2], Inge van der Werf[1,3], Livius Penter[4,5,6,7], Marijn A. Vermeulen[1], Farnaz Barneh[1], Alicia Perzolli[1,2], Joyce I. Meesters-Ensing[1], Marta Fiocco[1,8,9], Hester A. de Groot-Kruseman[1], Rubina Moeniralam[1], Kristina Bang Christensen[10], Billie Porter[11], Kathleen Pfaff[11], Jacqueline S. Garcia[4,6], Scott J. Rodig[13], Catherine J. Wu[4,5,6,12], Henrik Hasle[14], Stefan Nierkens[1,15], Mirjam E. Belderbos[1], C. Michel Zwaan[1,2#], Olaf Heidenreich[1,16#*]

[1]Princess Máxima Center for Pediatric Oncology, 3584 CS Utrecht, The Netherlands.
[2]Department of Pediatric Oncology, Erasmus MC/Sophia Children's Hospital, 3015 GD Rotterdam, The Netherlands.
[3]Oncode Institute, 3521 AL, Utrecht, The Netherlands
[4]Department of Medical Oncology, Dana-Farber Cancer Institute, Boston, MA, USA
[5]Broad Institute of Massachusetts Institute of Technology and Harvard University, Cambridge, MA, USA
[6]Harvard Medical School, Boston, MA, USA
[7]Department of Hematology, Oncology, and Tumorimmunology, Campus Virchow Klinikum, Berlin, Charité - Universitätsmedizin Berlin, Freie Universität Berlin and Humboldt-Universität zu Berlin, Berlin, Germany
[8]Mathematical Institute, Leiden University, Leiden, The Netherlands
[9]Department of Biomedical Data Sciences, Leiden University Medical Center, Leiden, The Netherlands.
[10]Department of Pathology, Aarhus University Hospital, Aarhus, Denmark
[11]Center for Immuno-Oncology, Dana-Farber Cancer Institute, Boston, MA, USA
[12]Department of Medicine, Brigham and Women's Hospital, Boston, MA, USA
[13]Department of Pathology, Brigham and Women's Hospital, Boston, MA, USA
[14]Pediatrics and Adolescent Medicine, Aarhus University Hospital, Aarhus, Denmark
[15]Center for Translational Immunology, University Medical Center Utrecht, 3584 CX Utrecht, The Netherlands.
[16]Wolfson Childhood Cancer Research Centre, Newcastle University, Newcastle upon Tyne NE1 7RU, UK.
[#]Equal contribution

*Corresponding author: Olaf Heidenreich, Princess Máxima Center for Pediatric Oncology, 3584 CS Utrecht, The Netherlands. Phone: 088-9727272; E-mail: o.t.heidenreich@prinsesmaximacentrum.nl

Running title: The spatial organization of immunity in pediatric AML

Disclosure of conflicts of interest:

J.S.G. reports serving on steering committee and receiving personal fees from AbbVie, Genentech, and Servier and institutional research funds from AbbVie, Genentech, Pfizer, and AstraZeneca.

S.R. receives research support from Bristol-Myers-Squibb and KITE/Gilead, and is a member of the SAB of Immunitas Therapeutics.

C.J.W. holds equity in BioNTech, Inc and receives research support from Pharmacyclics.

C.M.Z. receives institutional research support from Pfizer, Abbvie, Takeda, Jazz, Kura, Gilead, and Daiichi Sankyo, provides consultancy services for Kura, Bristol-Myers-Squibb, Novartis, Gilead, Incyte, and Syndax, and serves on advisory committees for Novartis, Sanofi, and Incyte.

O.H. receives institutional research support from Syndax and Roche.

The remaining authors declare no competing financial interests.

Figures/Tables: 5 Main Figures, 5 Supplementary Figures, 6 Supplementary Tables.

Words (excl. references): 6290 **References:** 74

Keywords: spatial transcriptomics, trephine, tertiary lymphoid structures, ectopic T cell networks, hematological malignancies.

Abstract:

Because of the low mutational burden, children with acute myeloid leukemia (AML) are thought to have a 'cold' tumor microenvironment and consequently, a low likelihood of response to T cell-directed immunotherapies. Here, we provide a multidimensional overview of the tumor immune microenvironment in newly diagnosed pediatric AML. On a cohort level, we demonstrate wide variation in T cell infiltration with nearly one-third of cases harboring an immune-infiltrated bone marrow. These immune-infiltrated cases are characterized by a decreased abundance of M2-like macrophages, which we find to be associated with response to T cell-directed immunotherapy in adult AML. On an organizational level, we reveal the composition of spatially organized immune aggregates in pediatric AML, and show that in the adult setting such aggregates in post-treatment bone marrow and extramedullary sites associate with response to ipilimumab-based therapy. Altogether, our study provides immune correlates of response to T cell-directed immunotherapies and indicates starting points for further investigations into immunomodulatory mechanisms in AML.

Statement of significance:

The limited response rates to T cell-directed immunotherapies remain a major challenge in AML. This study reveals the spatial organization of the tumor immune microenvironment in pediatric AML, identifies that immune aggregates associate with response to T cell-directed immunotherapy in the adult setting, and provides starting points for future investigations into immunomodulatory mechanisms in AML.

Introduction

An immune-infiltrated tumor microenvironment is of crucial importance to elicit responses to T cell-directed immunotherapies such as immune checkpoint inhibitors and bispecific antibodies[1]. Hence, patients with an immune-depleted or 'cold' tumor microenvironment show significantly reduced response rates[1]. Due to the low mutational burden and the associated poor immunogenicity of pediatric cancers such as acute myeloid leukemia, children are thought to be suboptimal candidates for T cell-directed immunotherapies[2-5]. Nonetheless, recent evidence suggests that considerable variation in immune cell infiltration exists among cancers that are considered to be immunologically 'cold'[6-8]. For instance, in adult AML, *TP53* mutations have been linked to increased levels of immune cell infiltration (i.e. increased T-, natural killer- (NK), and B cells) in the bone marrow (BM) and to improved responses following bispecific antibody treatment compared to *TP53*-wildtype AML[6-9]. Little is known about the immune compartment in the BM of pediatric AML and clinical trials that evaluate the efficacy of T cell-directed immunotherapies in the pediatric population have only recently been initiated (e.g., NCT03825367). Therefore, it is unclear whether pediatric AML may benefit from such immunotherapies. In addition, efforts in the field of solid cancers have shown that immunity in the tumor microenvironment is spatially organized with relevance for prognosis and immunotherapy response[10-13], while its relevance is unclear in hematological malignancies. This prompted us to perform a multidimensional characterization of the tumor immune microenvironment in treatment-naïve *de novo* pediatric AML and non-leukemic controls.

Here, we reveal wide variation in T cell abundance among pediatric AML cases with nearly one-third of cases harboring an immune-infiltrated BM. In immune-infiltrated cases, we show the presence of an activated T and NK cell response and a decreased abundance of anti-inflammatory M2-like macrophages. Furthermore, the M2-like macrophage abundance was predictive of response to T cell-directed immunotherapy in adult AML. Our integrative spatial analyses demonstrate the composition of spatially organized immune aggregates in the BM of pediatric AML, and identify such networks to be present in post-treatment BM and extramedullary sites of responders to ipilimumab-based therapy in the adult setting. Collectively, our study provides immune correlates of response to T cell-directed immunotherapies and indicates starting points for further investigations into immunomodulatory mechanisms in AML.

Results

A subset of pediatric AML patients has high T cell infiltration in the bone marrow

To determine whether the BM microenvironment in pediatric AML is characterized by high ('hot') or low ('cold') T cell infiltration, we performed immunohistochemistry (IHC) with antibodies against CD3 and CD8 on 82 formalin-fixed and paraffin-embedded (FFPE) BM biopsies from pediatric patients with treatment-naïve *de novo* AML (N=72), and age- and sex-matched non-leukemic individuals (N=10; **Fig. 1A**; representative images shown in **Fig. 1B-C**). Patient characteristics are depicted in **Table S1**. We found a trend towards a decreased abundance of the number of T cells and a significant decrease in $CD8^+$ T cells in pediatric AML cases in comparison to non-leukemic controls (P = 0.11 and P = 0.011, respectively; **Fig. 1D-E**), similar to other observations in adult and pediatric AML[5,14-15]. The T- and $CD8^+$ T cell infiltration ranged from 55 to 9,832 cells/mm^2 between individual pediatric AML cases, with a subset showing high T- and $CD8^+$ T cell infiltration in the BM (above median of non-leukemic controls; N=22 and N=18, respectively; **Fig. 1D-E**). Next, we explored whether this heterogeneity of T cell infiltration reflected inherent differences in disease biology. Remarkably, cases with complex karyotype AML had higher numbers of BM T cells compared to those with normal karyotype AML (P = 0.03; **Fig. 1F**). In addition, *KMT2A*-rearrangements were the most common cytogenetic alterations among cases with high $CD3^+$ and $CD8^+$ T cell abundance (n=11/22 and n=7/18, respectively; **Figure 1F-G**). Other clinical data including the abundance of leukemic blasts, AML differentiation stage (FAB-classification), or specific cytogenetic alterations did not correlate with T- and $CD8^+$ T cell infiltration (**Fig. 1F-G, Fig. S1A-D)**. These results indicate that other variables such as AML molecular aberrations (e.g., mutated NPM1 and WT-1) may be more relevant in shaping BM T cell infiltration[16]. However, AML molecular aberrations were not reported in the majority of cases (78%), which precluded meaningful analyses.

To validate the increased T cell infiltration in AML cases with complex karyotype compared to normal karyotype AML, we reanalyzed a large, publicly available, treatment-naïve pediatric AML cohort (TARGET, N=159 patients with matching clinical- and bulk BM RNA-sequencing (bulk RNA-seq) data)[17]. Utilizing the immune deconvolution tool CIBERSORTx[18-20], we estimated the abundance of total T- and $CD8^+$ T cells from bulk RNA-seq data. In the TARGET-AML cohort, the estimated abundance scores of T- and $CD8^+$ T cell infiltration ranged from 0.15 to 5.15 and 0 to 1.43, respectively. Since we did not have non-leukemic reference values for this cohort, we dichotomized patients into $CD3^+$- and $CD8^+$ T cell-high and -low groups using the median estimated BM $CD3^+$- and $CD8^+$ T cell abundance. In this dataset, we did not detect an increased number of BM T cells in complex compared to

normal karyotype AML (**Fig. 1H)**. Furthermore, we did not identify *KMT2A*-rearranged AML to be enriched among cases in the $CD3^+$ or $CD8^+$ T cell-high groups**,** nor did we find differences in the estimated T- and $CD8^+$ T cell abundance among other cytogenetic subgroups and AML differentiation stages (**Fig. 1H-I**, **Fig. S1E-F**). In contrast, there was a negative correlation, albeit subtle, between leukemic blasts and the estimated abundance of T cells (r = -0.24, P = 0.03; **Fig. S1G;** $CD8^+$ T cells shown in **Fig. S1H**). Like our dataset, AML molecular aberrations were not reported in the majority of cases (73%). In sum, we identified wide heterogeneity in T cell infiltration in the BM of pediatric AML with nearly one-third of cases (31%) showing notably high T cell infiltration. To understand whether pediatric AML cases with high BM T cell infiltration may represent a subgroup with enhanced susceptibility to immunotherapy, we decided to dissect their tumor immune microenvironment more deeply.

Immune-infiltrated leukemias are characterized by an activated T- and NK cell response

To further characterize the immune profiles of pediatric AML with a high abundance of T cells in the BM, we categorized AML cases into two groups using the non-leukemic controls' median $CD3^+$ T cell abundance as the cut-off value (1133 cells/mm^2). Focused IHC analyses of CD20 expression showed that patients in the $CD3^+$ T cell-high group also had a significantly higher abundance of $CD20^+$ B cells in comparison to the $CD3^+$ T cell-low group (P < 0.001; **Fig. 2A**). Accordingly, we termed the two groups 'immune-infiltrated' and 'immune-depleted' (N=22 and N=50, respectively). Next, we investigated whether these groups demonstrated differences in clinical outcomes upon standard chemotherapy treatment (intensive anthracycline- and cytarabine-based chemotherapy and allogeneic stem cell transplantation in selected high-risk cases[21]), as seen in many other cancer types[1]. We did not detect differences in overall survival between the immune-infiltrated and immune-depleted group (**Fig. S2A**). To increase statistical power to detect differences in survival between immune-infiltrated and immune-depleted AML cases, we repeated the analysis in the TARGET-AML cohort[17]. Again, we did not detect differences in overall survival between the immune-infiltrated ($CD3^+$ T cell-high, n=80) and immune-depleted ($CD3^+$ T cell-low, n=79) groups (**Fig. S2B**). However, cases with complex karyotype AML, which has been associated with inferior overall survival in pediatric AML, were overrepresented in the immune-infiltrated group (n=16 versus n=8 cases, respectively)[22]. We therefore performed a focused survival analysis in cases with complex karyotype AML. Strikingly, we found that immune-infiltrated cases had a significantly better overall survival in comparison to immune-depleted cases (P = 0.02; **Fig. 2B**), suggesting that BM immune features may play a role in outcomes following standard chemotherapy treatment in pediatric AML.

In addition to a potential role for BM immune infiltration in outcomes following standard chemotherapy, the presence of a pre-existing adaptive immune response could make patients receptive to T cell-directed immunotherapies[7-9,23-24]. To investigate whether such an immune response is present at diagnosis, we evaluated the expression of immune-related genes in a cytogenetically representative subset of immune-infiltrated (n=6) and immune-depleted cases (n=17) (**Table S1**) using the NanoString PanCancer IO 360™ panel (770 genes). We first focused on genes related to T- and NK cell activation and cytotoxicity, as these populations are central for tumor eradication[25]. In our cohort, immune-infiltrated cases showed significant upregulation of genes related to T- and NK cell activation and cytotoxicity including *CD28*, *ICOS*, *TNFRSF9* (encoding CD137), *KLRK1* (encoding NKG2D), *GZMA*, *GZMK*, *PRF1*, and *FASLG*; **Fig. 2C**). In addition, the immune checkpoint genes *TIGIT*, *LAG3*, *CTLA4*, and *PDCD1* (encoding PD-1) were significantly upregulated in comparison to immune-depleted cases, together indicating an activated T- and/or NK cell response (**Fig. 2C**)[26-28]. We further validated the increased expression of T- and NK cell activation, cytotoxicity, and immune checkpoint genes in immune-infiltrated compared to immune-depleted cases using the TARGET-AML cohort[17]. Similar to our cohort, cases in the immune-infiltrated group showed significant upregulation of *CD28*, *ICOS*, *KLRK1, GZMA*, *GZMK*, *PRF1, FASLG*, *TIGIT, LAG3*, and *CTLA4* in comparison to cases in the immune-depleted group (**Fig. S2C**; full list of differentially expressed genes shown in **Table S2**). In addition, genes related to NK cells (e.g., *KIR2DL1*, *KIR2DL2*, *KLRC1, KLRD1*) and B cells (e.g., *MS4A1*, *CD79A*, *IGHM*, *IGHG1*) were significantly upregulated in the immune-infiltrated group, suggesting an NK- and B cell-rich BM (**Fig. S2E**)[29-30]. Taken together, these results suggest an activated T- and NK cell response in pediatric AML cases with an immune-infiltrated BM.

M2-like macrophages are decreased in immune-infiltrated AML and predict response to T-cell directed immunotherapy

To elucidate mechanisms driving high- and low immune infiltration in the BM of pediatric AML, we investigated the expression of factors that either promote or restrict T cell infiltration. As anticipated, immune-infiltrated cases demonstrated significantly higher expression of genes related to T cell-attracting chemokines (*CXCL9*, *CXCL10*), and their corresponding receptor (*CXCR3*; **Fig. 2C**). In line with this, pathway analysis using the GO biological processes and WikiPathways gene sets indicated that immune-infiltrated cases were enriched in T cell migration and chemokine signaling, suggesting that immune-depleted cases lack signals that attract T cells to the BM (**Fig. 2D**; full list of pathways in **Table S3**). In solid cancers, macrophages have been described as key players in attracting T cells[31]. Specifically, pro-inflammatory M1-like macrophages are known to be a primary source of T cell-attracting chemokines, while anti-inflammatory M2-like macrophages restrict T cell infiltration into the

tumor[31-32]. Previously, a gene expression-based score that reflects the ratio between M2- and M1-like macrophages (a score > 0 indicates M2-predominance, while a score < 0 indicates M1-predominance; collectively termed M2-predominance score moving forward) has been developed for five cancer types including AML[33]. We applied this score to our cohort and found that the M2-predominance score was negatively correlated with the BM T- and $CD8^+$ T cell abundance (r = -0.75 [95% CI: -0.89 to -0.48], P < 0.001; r = -0.53 [95% CI: -0.76 to -0.12], P = 0.014, respectively; **Fig. 2E** and **Fig. S2D**). Concordantly, we identified a significantly decreased M2-predominance score in immune-infiltrated compared to immune-depleted cases (P = 0.001; **Fig. 2F**). In the TARGET-AML cohort, we detected an inverse correlation between the M2-predominance score and the T- and $CD8^+$ T cell abundance in the BM (r = -0.25 [95% CI: -0.39 to -0.10], P = 0.002; r = -0.20 [95% CI: -0.35 to -0.05], P = 0.011, respectively; **Fig. 2G** and **Fig. S2E**). Also, we observed a significantly decreased M2-predominance score in the immune-infiltrated in comparison to the immune-depleted group (P = 0.002; **Fig. 2H**).

While immunotherapy has revolutionized the outcome of B cell acute lymphoblastic leukemia and many other cancers[1,34], results from immunotherapy trials in AML have been very modest[7-9,23-24], indicating the need to identify biomarkers predictive of response. Therefore, we explored the potential of the M2-predominance score as a predictor of response to T cell-directed therapies. As gene expression data from immunotherapy-treated pediatric AML were not available, we used a BM immune-related gene expression profiling dataset of 30 relapsed or refractory adult AML cases prior to treatment with flotetuzumab, a bispecific CD3 x CD123 antibody, in the context of a clinical trial (CP-MGD006-01; NCT02152956)[7,9]. Strikingly, the M2-predominance score was significantly decreased in cases with anti-leukemic activity (n=12) in comparison to non-responders (n=18; P < 0.001; **Fig. 2I**). Notably, the M2-predominance score outperformed several other known predictors of response to immunotherapy (area under the receiver operating characteristic-curve: 0.854 [95% CI 0.71-0.99], P = 0.0012; **Fig. 2J**)[33,35]. Thus, we identified a decreased M2-predominance score in the BM of immune-infiltrated cases, and found that the M2-predominance score may be a potential biomarker of response to T cell-directed immunotherapies in adult AML, which should be validated in future immunotherapy trials in both adult and pediatric AML.

T cells cluster into spatially organized networks in the bone marrow of pediatric AML

Several studies in solid cancers have identified large, organized aggregates composed of T-, B-, and various other immune- and stromal cell subsets in the tumor microenvironment[36-38]. These aggregates, termed tertiary lymphoid structures (TLS), are thought to have a similar role as secondary lymphoid structures in priming of anti-cancer immune responses. Moreover, their presence has been associated with better responses to immunotherapy in many cancer

types[11-13,36-38]. As TLS often develop at sites of chronic inflammation, we asked whether similar structures were present in the BM of immune-infiltrated pediatric AML cases. Accordingly, we first investigated the number of T cell networks in pediatric immune-infiltrated, immune-depleted, and non-leukemic BM biopsies (N=22, N=50, and N=10, respectively). In this analysis, T cell networks were defined as at least 10 directly interacting T cells (≤10 µm between adjacent nuclei), to avoid classifying randomly dispersed T cells as networks (**Fig. 3A**)[39]. We found that T cell networks were present in both AML groups and in controls, although they were significantly more frequent in the BM of immune-infiltrated compared to immune-depleted cases ($P < 0.001$; **Fig. 3B** and **Table S1**). Moreover, controls had significantly more T cell networks in comparison to immune-depleted cases ($P = 0.027$; **Fig. 3B;** representative images of immune-depleted biopsies shown in **Fig. S3A-B**). Furthermore, a strong correlation was observed between the level of T cell infiltration and the number of T cell networks (N=82, $r = 0.91$ [95% CI: 0.85-0.94], $P < 0.001$; **Fig. 3C**).

In addition, we identified large T cell networks, defined as at least 100 directly interacting T cells, to be more abundant in the BM of immune-infiltrated compared to immune-depleted cases ($P < 0.001$; **Fig. 3D;** representative images of three immune-infiltrated biopsies shown in **Fig. 3E-G**). Interestingly, *KMT2A*-rearranged (9 out of 17 cases; 53%) and complex karyotype AML (3 out of 17 cases; 18%) were the most common cytogenetic subgroups among cases with large T cell networks (**Table S1**). These large networks often colocalized with a dense network of B cells in immune-infiltrated cases (seen in nine out of 15 immune-infiltrated cases (60%); representative images shown in **Fig. 3H-I, Fig. S3C-D**; none out of two immune-depleted cases). However, the large T cell networks identified in pediatric AML patients were not organized in a fashion seen in mature TLS with an inner zone of B cells surrounded by T cells (termed primary or secondary follicles)[37,40]. Instead, T- and B cells appeared to be mixed throughout the network, as seen in early or immature TLS and other immune aggregates (representative images shown in **Fig. 3H-I** and **Fig. S3C-D**)[37,40]. We did not identify these large networks in the BM of non-leukemic control biopsies (representative image shown in **Fig. S3F**). Taken together, these data show that spatially organized networks of T cells, both with and without colocalizing B cells, are widely abundant in treatment-naïve pediatric AML cases with an immune-infiltrated BM.

Composition of tertiary lymphoid structure-like aggregates in the bone marrow of pediatric AML

The identification of large T cell networks that colocalized with a dense network of B cells (for readability classified as ‘immune aggregates’), prompted us to explore whether the profiles of these networks shared similarities with TLS that have been reported in solid cancers (i.e. naive

B cells, plasma cells, several T cell subsets including follicular helper T cells, Tregs, and CD8$^+$ T cells, dendritic cells, high endothelial venules)[37]. To accurately identify TLS, several transcriptomic signatures have been proposed[38]: a 12-gene chemokine signature[41] ('12chem'; reflective of TLS independent of their maturation stage), an 8-gene follicular helper T cell signature[42] ('Tfh'; reflective of mature TLS), and a 29-gene TLS imprint signature[10] (reflective of mature TLS). To assess whether the immune aggregates identified in pediatric AML resembled TLS as seen in solid cancers, we aimed to examine the expression of these signatures in both immune aggregates and BM regions without such aggregates. We performed spatial transcriptomics using the GeoMx Digital Spatial Profiling platform[43] on eight BM biopsies: four immune-infiltrated AML biopsies with immune aggregates, and four reference biopsies (two immune-infiltrated AML biopsies without immune aggregates and two non-leukemic control biopsies; patient characteristics related to these biopsies are depicted in **Table S1**). Regions of interest (ROIs) included areas with immune aggregates, 'mixed' areas containing AML cells and various other populations, and 'control' areas in the non-leukemic BM (region types are illustrated in **Fig. 4A-C**). In total, we successfully sequenced 143 regions with an average of 335 cells per region (range: 126 to 826 cells): 35 immune aggregate regions, 92 mixed regions, and 16 control regions. Our analysis revealed two main clusters of regions in the UMAP: cluster 1 contained both regions with immune aggregates and mixed regions from biopsies with immune aggregates, while cluster 2 consisted of mixed regions from biopsies without these aggregates, and control regions (**Fig. 4D**). Consequently, we divided mixed regions in two distinct groups: areas from biopsies with immune aggregates (MIXED1, n=48), and those from biopsies without such aggregates (MIXED2, n=44). All three TLS-specific gene signatures were significantly enriched in immune aggregate regions in comparison to both mixed- and control regions (**Fig. 4E-G**). Thus, while the identified immune aggregates lacked the typical organization of mature TLS, we did identify enrichment of the Tfh- and TLS imprint signatures representative of mature TLS.

To gain insight into differences in the abundance of immune and stromal cell types between immune aggregate- and other BM regions, we performed immune deconvolution by integrating spatial transcriptomic data with single-cell RNA-sequencing- (scRNA-seq) and flow-sorted bulk RNA-seq data of microenvironmental cell populations[44]. Immune aggregate regions showed a significantly increased abundance of memory CD8$^+$ T cells, regulatory T cells (Tregs), plasma cells, and macrophages in comparison to both mixed- and control regions (**Fig. 4H-K)**. When considering macrophage polarization, we observed a significantly decreased M2-predominance score in immune aggregate regions in comparison to both mixed regions (**Fig. 4L)**. Furthermore, immune aggregate regions contained significantly more naïve B cells, endothelial cells, and fibroblasts compared to MIXED1-regions, underlining the distinct

composition of these aggregates in comparison to neighboring regions (**Fig. S4A-C**). In contrast, MIXED2 regions had a significantly higher abundance of neutrophils in comparison to both immune aggregate and MIXED1 regions (**Fig. S4D**). Albeit significantly enriched in comparison to control regions, NK cells and plasmacytoid dendritic cells (DCs) did not differ among regions in the AML biopsies (**Fig. S4E-F**). Additionally, immune aggregate regions did not show an increase in naïve $CD4^+$ T- and $CD8^+$ T cells (**Fig. S4G-H**). Lastly, myeloid DCs were enriched in both immune aggregate- and MIXED1 regions in comparison to MIXED2- and control regions (**Fig. 4I**). Collectively, our data suggest that the detected immune aggregates in the BM of pediatric AML patients share a cellular composition resembling that of TLS found in solid cancers. Given the absence of clear T- and B cell zones within the AML BM immune aggregates, and considering that TLS typically originate in non-lymphoid tissues, we will refer to these regions as TLS-like aggregates moving forward[7].

TLS-associated Tregs have been shown to actively suppress anti-tumor T cell responses in a mouse model of lung cancer[45]. Moreover, they have been found to attenuate the positive prognostic effect of TLS-associated $CD8^+$ T cells in human non-small cell lung cancer, colorectal cancer, and soft-tissue sarcoma[13,46-47]. Given that we observed wide infiltration of Tregs in TLS-like aggregates, we set out to determine whether this affected the activation status of $CD8^+$ T cells. To investigate this, we used an additional scRNA-seq reference profile specific for activated and resting BM T cells[44] and determined whether the fraction of activated $CD8^+$ T cells differed among region types. Remarkably, despite the high abundance of Tregs, TLS-like aggregates had similar proportions of activated $CD8^+$ T cells as both mixed regions, and a significantly higher proportion in comparison to control regions (**Fig. S4J-K;** absolute abundance shown in **Fig. S4L**). In sum, TLS-like aggregates, although highly infiltrated with Tregs, represent hotspots of activated $CD8^+$ T cells in the BM of immune-infiltrated pediatric AML.

Large T cell networks in AML bone marrow and extramedullary sites are present in responders after ipilimumab-based therapy

Given that TLS represent sites of intratumoral immune priming that can lead to successful anti-tumor immunity in solid cancers, they may also serve as markers of leukemia-specific immune responses in hematological malignancies[37,48-49]. Consequently, we aimed to evaluate whether T cell-directed immunotherapies could induce TLS-like aggregates in AML. As data from pediatric AML treated with such therapies were not available, we analyzed immunofluorescence data acquired from pre- and/or post-treatment biopsies of 11 transplant-naïve and post-transplant adult AML cases treated with ipilimumab-based therapy in the context of two clinical trials (ipilimumab with (ETCTN 10026 - NCT02890329)[50,51] or without

decitabine (ETCTN 9204 - NCT01822509)[20,52]; **Fig. 5A**). Using multiplex immunofluorescence data with antibodies against CD3, CD20, and CD34, we first investigated the presence of (large) T cell networks in longitudinal BM biopsies in three responders and three non-responders (**Fig. 5A**; n=18 BM biopsies in total; patient characteristics are depicted in **Table S4**). In four out of six cases, there was an increase in the number of T cell networks after treatment in both responders and non-responders (**Fig. 5B-C, E-F)**. However, large T cell networks with more than 100 T cells in post-treatment BM biopsies were only seen in responders (**Fig. 5B-D**). In addition, two responders and one non-responder had large T cell networks in the pre-treatment BM (**Fig. 5B,D,F**). Notably, a remarkably high level of (large) T cell networks before treatment was observed in one exceptional responder with sustained remission > 4.8 years following ipilimumab and decitabine treatment, consistent with an activated AML-specific immune response (**Fig. 5D**). Next, we aimed to assess whether these large T cell networks (n=43 networks among six BM biopsies) showed an enrichment of B cells, as observed in pediatric AML. We measured $CD20^+$ B cell density inside large T cell networks and in the total biopsy. Overall, the B cell density in large T cell networks was higher in comparison to that in total biopsy areas (P = 0.016; **Fig. 5H**). However, it is worth noting that >50% of these networks had no (n=22) or hardly any (n=1; 66 cells/mm^2) B cells, indicating the presence of large T cell networks with and without colocalizing B cells (representative images shown in **Fig. 5I-J** and **Fig. S5A-B**). Like pediatric AML, T and B cells in large T cell networks enriched with B cells were not organized in distinct zones (**Fig. 5I-J**). Furthermore, large T cell networks in pre-treatment biopsies did not differ in B cell density in comparison to post-treatment biopsies (P = 0.49; **Fig. S5C**). Taken together, we show that large T cell networks with and without colocalizing B cells are present in post-treatment BM biopsies of responders but not in non-responders to ipilimumab-based therapy.

Across the ETCTN 9204 and 10026 studies, extramedullary AML seemed to be characterized by particular sensitivity to CTLA-4 blockade, with two durable remissions in leukemia cutis and multiple other transient responses[50,52]. As we observed large T cell networks in the BM of responders after ipilimumab-based therapy, we asked whether these were also detectable in cases of sole extramedullary AML (two matched pre- and post-treatment biopsies, two pre-treatment biopsies, and one post-treatment biopsy were available; patient characteristics are depicted in **Table S4**). Through reanalysis of previously acquired immunofluorescence data (CD3)[51], we found that all three post-treatment biopsies contained large T cell networks, while none were present in the four pre-treatment biopsies (**Fig. S5D**; representative, matched pre- and post-treatment biopsies are shown in **Fig. S5E-F**). Thus, like the observations in post-treatment BM biopsies of responders to ipilimumab-based therapy, we identified large T cell networks in all extramedullary AML post-treatment biopsies

that responded to ipilimumab monotherapy. These results therefore suggest a role for large T cell networks in anti-tumor immune responses following ipilimumab-based therapy.

Discussion

The presence of a pre-existing immune infiltrate has been associated with response to T cell-directed immunotherapies in both solid and hematological cancers including adult AML[1,7-9,23-24,53]. However, clinical trials with T cell-directed immunotherapies have only recently been initiated for pediatric AML and because of the limited knowledge about the immune compartment in the BM of pediatric AML[54] (reviewed in ref. 55), it is unclear whether pediatric AML is generally susceptible to these therapies. Here, we performed a systematic assessment of the tumor immune microenvironment in pediatric AML including its spatial organization and demonstrated that nearly one-third of pediatric AML cases had an immune-infiltrated BM. These immune-infiltrated cases were characterized by a decreased abundance of M2-like macrophages, which we found to be associated with response to T cell-directed immunotherapy in adult AML. We further detected the presence of large spatially organized networks of T cells in the BM, dissected their cellular composition in pediatric AML using spatial transcriptomics, and showed that in the adult setting such networks are associated with response to ipilimumab-based therapy in post-treatment BM and extramedullary sites. Collectively, our study provides immune correlates of response to T cell-directed immunotherapies and indicates starting points for further investigations into immunomodulatory mechanisms in AML.

Although we identified a subset with high abundance of T cells, many pediatric AML cases had an immune-depleted BM microenvironment. Uncovering the underlying mechanisms that orchestrate immune infiltration in the AML BM is of crucial importance for the design of therapeutic strategies that turn ‘cold’ into ‘hot’ tumors[56]. In immune-infiltrated cases, we identified a decreased abundance of M2-like macrophages in comparison to their ‘cold’ counterparts, suggesting a role for M2-like macrophages in limiting T cell infiltration to the leukemic BM[31]. Consequently, targeting M2-like macrophages (e.g., using checkpoint blockade) to overcome their immunosuppressive functions could be an attractive therapeutic strategy for immune-depleted AML[57]. In addition, the identified association between the M2-like macrophage abundance and response to flotetuzumab in the adult setting may help with the identification of patients that are likely to respond to T cell-directed immunotherapy. As immune-infiltrated pediatric AML cases had an activated T and NK cell response and a decreased abundance of M2-like macrophages, such patients may indeed benefit from T cell-directed immunotherapies and clinical evaluation of these agents in the pediatric population is warranted.

Furthermore, our integrative spatial analyses showed that T cells in the BM can be organized into multicellular aggregates. Although TLS-like aggregates did not contain distinct T- and B cell zones typically seen in mature TLS in solid cancers, the localized enrichment of naïve B cells, plasma cells, and gene signatures reflective of mature TLS suggests that these aggregates are sites of full B cell maturation[38]. Additionally, the high abundance of memory $CD8^+$ T cells in these aggregates is consistent with the suspected role of TLS as sites of T cell differentiation[36-38]. Remarkably, although Tregs were enriched in TLS-like aggregates, these sites had a notably high abundance of activated $CD8^+$ T cells, indicating potent immune activation in these aggregates. In addition to TLS-like aggregates, we detected large T cell networks that lacked B cells. As such networks have also been associated with immunotherapy response in solid cancers, further investigations into the different types of immune aggregates in AML and their relevance for immunotherapy response are justified[39,58-59].

Finally, our exploratory analysis in matched pre- and post-treatment BM biopsies of adult AML cases treated with ipilimumab-based therapy demonstrated large T cell networks, both with and without colocalizing B cells, in post-treatment BM biopsies of responders but not in non-responders. These results are in line with a spatial proteomics effort in adult AML cases treated with flotetuzumab, which showed that two responders had T cell networks in post-treatment BM biopsies[7]. Furthermore, in AML cases with extramedullary AML treated with ipilimumab monotherapy, we observed a similar enrichment of large T cell networks in post-treatment biopsies of responders, further supporting a role for such immune aggregates in anti-tumor immune responses. Although TLS are considered to be sites where tumor-specific T- and B cell immune responses may be generated[36-38], we were unable to determine the tumor-specificity of these populations in TLS-like aggregates due to technical limitations associated with the FFPE nature of the biopsies. Novel developments in the field of spatial transcriptomics that allow for T- and B cell receptor clonality assessment promise to clarify target antigens of TLS in the future[60-61].

Altogether, our analyses deepen the understanding of the spatial organization of the BM immune microenvironment in AML and provides an impetus to explore how intratumoral immune aggregates could be exploited for improving immunotherapy outcomes. Further, our work provides a framework for leveraging spatial transcriptomics to interrogate the spatial organization of the leukemic BM. Advances in spatial transcriptomic techniques now allow for investigating the spatial dimension of hematological malignancies at single-cell resolution, opening an exciting path towards new discoveries in the field of AML[62-63].

Methods

Ethical regulation

This study complies with all relevant ethical regulations and was approved by the Institutional Review Boards of the Princess Máxima Center for Pediatric Oncology (PMCLAB2021.207 & PMCLAB2021.238), the Scientific Committee of the Dutch Nationwide Pathology Databank (PALGA: lzv2021-82)[64] and at participating sites of the ETCTN/CTEP 9204 and 10026 studies after written informed consent was obtained[50,52]. All patients treated at the Princess Máxima Center and Aarhus University Hospital provided written consent for banking and research use of these specimens, according to the Declaration of Helsinki. BM biopsy tissues acquired from external biobanks (n=28) were leftover material from standard care procedures and therefore, no informed consent was acquired, according to Dutch legislation and the code of conduct of the Committee on Regulation of Health Research (COREON).

Human patient samples

FFPE BM biopsies taken from the crista of children with treatment-naïve *de novo* AML were obtained from the Princess Máxima Center Biobank (n=15), biobanks of 10 other Dutch hospitals (n=28), mediated by the Dutch National Tissue Portal, and the biobank of Aarhus University Hospital (n=29). As controls, FFPE BM biopsies of age- and sex-matched children with treatment-naïve early-stage rhabdomyosarcoma were obtained from the Princess Máxima Center Biobank (n=10; non-leukemic controls). An experienced hemato-onco pathologist confirmed that these control biopsies resembled normal hematopoiesis and that there was no malignancy infiltrating the BM. BM and extramedullary biopsies of adult AML cases treated on ETCTN/CTEP 9204 and 10026 studies were collected at Dana-Farber Cancer Institute[50,51].

Immunohistochemistry/immunofluorescence and digital image analysis

BM and extramedullary biopsies of pediatric and adult AML cases were cut into consecutive sections of 4 and 5 µm, respectively. Conventional IHC was performed for CD3 (T cells), CD3-CD4 (duplex; for $CD4^+$ T cells and $CD4^+$ AML cells), CD8 (mainly $CD8^+$ T cells but may also stain rare $CD8^+$ NK- and dendritic cells), CD20 (B cells), CD34, CD117, and CD15 (immunophenotype-based AML markers) on pediatric AML BM biopsies using a Ventana Benchmark Ultra (Roche, Basel, Switzerland) automated staining instrument according to manufacturers' recommendations. A list of antibodies and suppliers is available in **Table S5**. Digital scans of stained slides were obtained using a NanoZoomer scanner (Hamamatsu, Shizuoka, Japan). Multiplex immunofluorescence using DAPI and antibodies against CD3 (T cells), CD20 (B cells), and CD34 (AML blasts and endothelial cells) was performed on pre-

and post-treatment BM biopsies of adult AML cases treated with ipilimumab-based therapy on the 10026 studies and imaged as previously described[20]. Staining of the biopsies was completed on a BOND RX fully automated stainer (Leica Biosystems, Nußloch, Germany) after baking tissue sections for 3 hours at 60°C. The BOND RX then performed deparaffinization and rehydration with series of graded ethanol to deionized water. Subsequently, antigen retrieval was performed utilizing Epitope Retrieval Solution 1 (pH 6) or 2 (pH 9), as shown in **Table S6** (ER1, ER2, Leica Biosystems, Cat. AR9961, AR9640). The secondary antibodies that were used are described in **Table S6** as well. The antibody complex was incubated for 10 minutes with its corresponding Opal Fluorophore Reagent (Akoya Biosciences, Marlborough, MA, USA) for signal visualization. After the final fluorophore application, the samples were incubated in Spectral DAPI solution (Akoya) for 10 minutes. Lastly, samples were removed from the BOND, air-dried, and mounted using Prolong Diamond Anti-fade mounting medium (Life Technologies, Cat. P3695). Whole-slide images have been obtained using the PhenoImager HT multispectral imaging platform (Akoya), were spectrally unmixed (Inform 2.6, Akoya), and 20x regions were stitched together (QuPath, v0.3.2.)[62]. Immunofluorescence data with DAPI and CD3 performed on extramedullary biopsies was acquired from previously published work[51]. For all imaged slides, whole-slide digital image analysis was performed in QuPath[65]. Inside QuPath, the deep learning-based cell segmentation tool StarDist and the machine learning-based Random Trees classifier were used to quantify the number of positive cells per mm^2 [65-66]. T cell networks were defined as at least 10 directly interacting $CD3^+$ T cells (≤ 10 µm between adjacent nuclei), detected using Delaunay Triangulation, and normalized per cm^2 [39,65,67]. Large T cell networks were defined as at least 100 directly interacting T cells. In adult AML BM biopsies, the density of $CD20^+$ B cells was measured inside large T cell network regions and in the total biopsy area (including the large T cell network regions).

Immune-related gene expression profiling

Four consecutive sections of 10 µm from six immune-infiltrated and 17 immune-depleted FFPE BM biopsies from a cytogenetically representative cohort of pediatric AML cases (patient characteristics in **Table S1**) were used to isolate RNA and to perform immune-related gene expression profiling with the 770-gene PanCancer IO 360 panel, as previously described (NanoString, Seattle, WA, USA)[7-9,30]. After passing quality control, raw data were normalized using ROSALIND® according to NanoString's recommendations (https://rosalind.bio/; San Diego, CA, USA). Normalized data were uploaded to the online iDEP platform and differentially expressed genes between immune-infiltrated and immune-depleted biopsies were identified using *DEseq2* with a false-discovery rate (FDR) cut-off of 0.05 and a minimum fold change of 2 (integrative Differential Expression and Pathway analysis;

http://bioinformatics.sdstate.edu/idep96/; V.0.96)[68]. Pathway analysis was performed using single-sample gene set enrichment analysis with the GO Biological Processes and WikiPathways gene sets with an FDR cut-off of 0.05[69-71]. The M2-predominance score was estimated using a published gene signature of M2-like macrophages compared to M1-like macrophages, inside the TIDE environment (tide.dfci.harvard.edu/)[33,72]. Similarly, the T cell inflamed gene expression profile, the CD8-, IFN-*γ*-, and TIDE scores were all calculated using TIDE[33].

GeoMx Digital Spatial Profiling

5 µm thick FFPE BM biopsy sections from six pediatric AML cases with an immune-infiltrated BM and two non-leukemic controls were put on three different slides and prepared for GeoMx Digital Spatial Profiling (DSP; NanoString), as previously described[43]. Slides were simultaneously incubated with immunofluorescent antibodies and GeoMx Whole Transcriptome Atlas profiling reagents. SYTO13 (S7575, Thermo Fisher,) was used for identification of nuclei, CD45 (NBP2-34528, Novus) for leukocytes, and CD3 (NBP2-54392AF647, Novus) for T cells. Stained slides were loaded onto the GeoMx instrument and scanned. ROIs were selected using the above-mentioned antibodies in combination with overlayed images of CD20, CD34, CD3-CD4 (duplex), and CD117 (IHC). Then, UV-photocleaved oligonucleotides were collected in separate wells and sequenced on the Nextseq2000 (Illumina, San Diego, CA, USA). Raw data were normalized using Quartile 3 count (Q3) normalization in R (V.4.2.1) as per NanoString's recommendations (code is available in the vignette of the *Geomxtools* package: https://bioconductor.org/packages/release/workflows/vignettes/GeoMxWorkflows/inst/doc/GeomxTools_RNA-NGS_Analysis.html). Batch correction was performed using Combat-seq[73]. Spatial Deconvolution was performed in the GeoMx DSP Analysis Suite using both the safeTME and healthy adult BM T cell reference profiles (*SpatialDecon* package; cell reference profiles are available via https://github.com/Nanostring-Biostats/CellProfileLibrary/blob/archive/safeTME-for-tumor-immune.csv and https://github.com/Nanostring-Biostats/CellProfileLibrary/blob/archive/Tcell_Adult_BoneMarrow_10x.csv)[44]. Deconvoluted abundance scores were normalized for ROI-size and, in case of immune aggregates, for the ROI-area covered by these aggregates. The '12chem', 'Tfh', and 'TLS imprint', and M2-predominance signatures were applied to Q3-normalized data and further normalized as mentioned above[10,33,41-42].

External pediatric and adult AML datasets

Bulk RNA-seq data (counts and transcripts-per-million; TPM) and matching clinical data of 159 treatment-naïve *de novo* pediatric AML cases generated as part of the TARGET-AML project was acquired via https://www.cBioportal.org[17,74]. TPM values were used to estimate the abundance of total T- and $CD8^+$ T cells using CIBERSORTx, as described previously (LM22 reference profile; https://cibersortx.stanford.edu/)[18-20]. Count values were used to determine differentially expressed genes between immune-infiltrated and immune-depleted cases, as described above[68]. Immune-related gene expression data (PanCancer IO 360™ panel) from pre-treatment BM of 30 relapsed or refractory adult AML cases that were treated with flotetuzumab in the context of the CP-MGD006-01 clinical trial (NCT02152956)[7-9] were kindly provided by Professor Sergio Rutella (Nottingham Trent University, England) and dr. Patrick Kaminker (MacroGenics, Rockville, MD, USA) and analyzed as described above.

Statistical analyses

Statistical analyses were performed with GraphPad Prism V.9.3.0 (GraphPad Software, LA Jolla, CA, USA). In case of no Gaussian distribution, differences between two independent groups and two paired groups were compared using the Mann-Whitney test and the Wilcoxon paired signed-rank test, respectively. For Gaussian-distributed data, unpaired and paired t-tests, respectively, were used. The correlation between two variables was evaluated using Spearman's *r*. To measure the area under the receiver operating characteristic curve, we employed the Wilson-Brown method. To estimate the survival from diagnosis, the Kaplan-Meier's methodology was employed. To assess the difference between survival estimates in different groups, the log rank test was used. In case of multiple comparisons and no Gaussian distribution of residuals, we employed the Kruskal-Wallis test followed by Dunn's test for multiple comparisons including a Bonferroni correction. For spatial transcriptomics data, $P < 0.01$ was considered statistically significant to correct for measuring multiple regions from the same biopsy. For all the other comparisons, $P < 0.05$ was considered statistically significant.

Data availability

Sequencing data can be accessed from the Gene Expression Omnibus (nCounter data: GSEXXX; GeoMx data: GSEXXX; both normalized counts [GSE IDs will be available upon approval]) and from the European Genome-phenome Archive (EGA) database (https://ega-archive.org/studies/EGAXXX; raw nCounter and GeoMx data [idem]).

Acknowledgements

We would like to thank all patients and/or their families for their generous consent for the research use of these samples; the staff of the University Medical Center Utrecht Tissue Facility for their excellent immunohistochemistry service (Domenico Castigliego, Petra van der Weide, Petra van der Kraak, Erica Siera, Karina Timmer, Sven van Kempen), and the team at Utrecht Sequencing Facility for performing the NanoString experiments (nCounter and GeoMx) and for providing assistance with data-analysis (dr. Ies Nijman, Robin Geene, Pim Kloosterman); Professor Sergio Rutella (Notthingham Trent University) and dr. Patrick Kaminker (MacroGenics) for providing us with BM immune-related gene expression data of immunotherapy-treated adult AML cases; Dr. Matthew S. Davids for clinical data of patients treated on ETCTN/CTEP 9204; Dr. Ivette Deckers and dr. Annette Gijsbers (PALGA) performed essential work for the acquisition of bone biopsies from other hospitals; prof. dr. Gertjan Kaspers and dr. Bianca Goemans aided with identifying potential patients, the biobank staff (Jantien Woudstra, Marion Koopmans, dr. Edwin Sonneveld) helped to identify patient material, and Arie Maat aided with the sectioning of bone biopsy sections; dr. Caroline Lindemans, members from the Heidenreich group (dr. Katarzyna Szoltysek, dr. Farnaz Barneh, dr. Mauricio Ferrao-Blanco, Elizabeth Schweighart, Nina van der Wilt), the Van Heesch group (dr. Ana Pinheiro-Lopes), and the single-cell sequencing facility (dr. Lindy Visser) at the Princess Máxima Center for Pediatric Oncology for carefully reading the manuscript and/or fruitful discussions. Figure 1A, 3A, 4A-C, and 5A have been created using BioRender.com

This work has been funded in part by a KIKA (329) program grant to O.H. L.P. is a Scholar of the American Society of Hematology, participant in the BIH Charité Digital Clinician Scientist Program funded by the DFG, the Charité – Universitätsmedizin Berlin, and the Berlin Institute of Health at Charité (BIH) and is supported by the Max-Eder program of the German Cancer Aid. J.S.G. is supported by the Conquer Cancer Foundation Career Development Award, Leukemia and Lymphoma Society Translational Research Program Award, and NIH K08CA245209. NCI CTEP provided study drug (Ipilimumab) support.

This work was supported by National Institutes of Health, National Cancer Institute grant P01CA229092 (C.J.W.), UM1CA186709 (Principal Investigator: Geoffrey Shapiro), National Cancer Institute Cancer Therapy Evaluation Program, Bristol-Myers Squibb, and LLS Therapy Accelerator Program. This work was further supported by the CIMAC-CIDC Network. Scientific and financial support for the CIMAC-CIDC Network is provided through National Institutes of Health, National Cancer Institute Cooperative Agreements U24CA224319 (to the Icahn School of Medicine at Mount Sinai CIMAC), U24CA224331 (to the Dana-Farber Cancer Institute CIMAC), U24CA224285 (to the MD Anderson Cancer Center CIMAC), U24CA224309 (to the Stanford University CIMAC), and U24CA224316 (to the CIDC at Dana-Farber Cancer Institute). The CIMAC-CIDC website is found at https://cimac-network.org/.

Author contributions

Conceptualization: J.B.K, I.W., M.A.V., S.N., M.B., C.M.Z., O.H. Methodology: J.B.K, I.W., M.A.V., M.F., S.N., M.B., C.M.Z., O.H. Data acquisition: J.B.K., M.A.V., F.B., J.I.M.-E. H.G.-K., R.M, K.B.C., B.P., K.P., H.H. Data analysis and interpretation: J.B.K., I.W., L.P., F.B., A.P., J.I.M.-E., J.S.G., S.J.R., C.J.W., H.H. Writing – Original Draft: J.B.K.; Writing – Reviewing & Editing: all authors; Supervision: S.N., M.B., C.M.Z., O.H.

References

1. Bruni D, Angell HK, Galon J. The immune contexture and Immunoscore in cancer prognosis and therapeutic efficacy. *Nat Rev Cancer*. 2020;20(11):662-680.
2. Gröbner SN, Worst BC, Weischenfeldt J, Buchhalter I, Kleinheinz K, Rudneva VA, et al. The landscape of genomic alterations across childhood cancers. *Nature*. 2018;555(7696):321-327.
3. Majzner RG, Heitzeneder S, Mackall CL. Harnessing the Immunotherapy Revolution for the Treatment of Childhood Cancers. *Cancer Cell*. 2017;31(4):476-485.
4. Pfister SM, Reyes-Múgica M, Chan JKC, Hasle H, Lazar AJ, Rossi S, et al. A Summary of the Inaugural WHO Classification of Pediatric Tumors: Transitioning from the Optical into the Molecular Era. *Cancer Discov*. 2022;12(2):331-355.
5. Lasry A, Nadorp B, Fornerod M, Nicolet D, Wu H, Walker CJ, et al. An inflammatory state remodels the immune microenvironment and improves risk stratification in acute myeloid leukemia. Nat Cancer. 2023 Jan;4(1):27-42.
6. Dufva O, Pölönen P, Brück O, Keränen MAI, Klievink J, Mehtonen J, et al. Immunogenomic Landscape of Hematological Malignancies. *Cancer Cell*. 2020;38(3):380-399.e13.
7. Vadakekolathu J, Minden MD, Hood T, Church SE, Reeder S, Altmann H, et al. Immune landscapes predict chemotherapy resistance and immunotherapy response in acute myeloid leukemia. *Sci Transl Med*. 2020;12(546):eaaz0463.
8. Vadakekolathu J, Lai C, Reeder S, Church SE, Hood T, Lourdusamy A, et al. TP53 abnormalities correlate with immune infiltration and associate with response to flotetuzumab immunotherapy in AML. *Blood Adv*. 2020;4(20):5011-5024.
9. Uy GL, Aldoss I, Foster MC, Sayre PH, Wieduwilt MJ, Advani AS, et al. Flotetuzumab as salvage immunotherapy for refractory acute myeloid leukemia. Blood. 2021 Feb 11;137(6):751-762.
10. Meylan M, Petitprez F, Becht E, Bougoüin A, Pupier G, Calvez A, et al. Tertiary lymphoid structures generate and propagate anti-tumor antibody-producing plasma cells in renal cell cancer. *Immunity*. S2022;55(3):527-541.e5.
11. Helmink BA, Reddy SM, Gao J, Zhang S, Basar R, Thakur R, et al. B cells and tertiary lymphoid structures promote immunotherapy response. Nature. 2020 Jan;577(7791):549-555.
12. Vanhersecke L, Brunet M, Guégan JP, Rey C, Bougouin A, Cousin S, et al. Mature tertiary lymphoid structures predict immune checkpoint inhibitor efficacy in solid tumors independently of PD-L1 expression. Nat Cancer. 2021 Aug;2(8):794-802.
13. Italiano A, Bessede A, Pulido M, Bompas E, Piperno-Neumann S, Chevreau C, et al. Pembrolizumab in soft-tissue sarcomas with tertiary lymphoid structures: a phase 2 PEMBROSARC trial cohort. *Nat Med*. 2022;28(6):1199-1206.
14. van Galen P, Hovestadt V, Wadsworth Ii MH, Hughes TK, Griffin GK, Battaglia S, et al. Single-Cell RNA-Seq Reveals AML Hierarchies Relevant to Disease Progression and Immunity. Cell. 2019 Mar 7;176(6):1265-1281.e24.
15. Brück O, Dufva O, Hohtari H, Blom S, Turkki R, Ilander M, et al. Immune profiles in acute myeloid leukemia bone marrow associate with patient age, T-cell receptor clonality, and survival. Blood Adv. 2020 Jan 28;4(2):274-286.
16. Austin RJ, Straube J, Halder R, Janardhanan Y, Bruedigam C, Witkowski M, et al. Oncogenic drivers dictate immune control of acute myeloid leukemia. Nat Commun. 2023 Apr 14;14(1):2155.

17. Bolouri H, Farrar JE, Triche T Jr, Ries RE, Lim EL, Alonzo TA, et al. The molecular landscape of pediatric acute myeloid leukemia reveals recurrent structural alterations and age-specific mutational interactions. *Nat Med*. 2018;24(1):103-112.
18. Newman AM, Steen CB, Liu CL, Gentles AJ, Chaudhuri AA, Scherer F, et al. Determining cell type abundance and expression from bulk tissues with digital cytometry. Nat Biotechnol. 2019 Jul;37(7):773-782.
19. Wang Y, Cai YY, Herold T, Nie RC, Zhang Y, Gale RP, et al. An Immune Risk Score Predicts Survival of Patients with Acute Myeloid Leukemia Receiving Chemotherapy. Clin Cancer Res. 2021 Jan 1;27(1):255-266.
20. Penter L, Liu Y, Wolff JO, Yang L, Taing L, Jhaveri A, et al. Mechanisms of response and resistance to combined decitabine and ipilimumab for advanced myeloid disease. Blood. 2023 Apr 13;141(15):1817-1830.
21. de Rooij JD, Zwaan CM, van den Heuvel-Eibrink M. Pediatric AML: From Biology to Clinical Management. J Clin Med. 2015 Jan 9;4(1):127-49. doi: 10.3390/jcm4010127.
22. Bager N, Juul-Dam KL, Sandahl JD, Abrahamsson J, Beverloo B, de Bont ESJM, et al. Complex and monosomal karyotype are distinct cytogenetic entities with an adverse prognostic impact in paediatric acute myeloid leukaemia. A NOPHO-DBH-AML study. Br J Haematol. 2018 Nov;183(4):618-628.
23. Daver N, Garcia-Manero G, Basu S, Boddu PC, Alfayez M, Cortes JE, et al. Efficacy, Safety, and Biomarkers of Response to Azacitidine and Nivolumab in Relapsed/Refractory Acute Myeloid Leukemia: A Nonrandomized, Open-Label, Phase II Study. Cancer Discov. 2019 Mar;9(3):370-383.
24. Vadakekolathu J, Rutella S. Escape from T-cell targeting immunotherapies in acute myeloid leukemia. Blood. 2023 Jul 19:blood.2023019961.
25. Joyce JA, Fearon DT. T cell exclusion, immune privilege, and the tumor microenvironment. Science. 2015 Apr 3;348(6230):74-80.
26. Ye Q, Song DG, Poussin M, Yamamoto T, Best A, Li C, et al. CD137 accurately identifies and enriches for naturally occurring tumor-reactive T cells in tumor. Clin Cancer Res. 2014 Jan 1;20(1):44-55.
27. North J, Bakhsh I, Marden C, Pittman H, Addison E, Navarrete C, et al. Tumor-primed human natural killer cells lyse NK-resistant tumor targets: evidence of a two-stage process in resting NK cell activation. J Immunol. 2007 Jan 1;178(1):85-94.
28. Oestreich KJ, Yoon H, Ahmed R, Boss JM. NFATc1 regulates PD-1 expression upon T cell activation. J Immunol. 2008 Oct 1;181(7):4832-9.
29. Pereira BI, De Maeyer RPH, Covre LP, Nehar-Belaid D, Lanna A, Ward S, et al. Sestrins induce natural killer function in senescent-like $CD8^+$ T cells. Nat Immunol. 2020 Jun;21(6):684-694.
30. Danaher P, Warren S, Dennis L, D'Amico L, White A, Disis ML, et al. Gene expression markers of Tumor Infiltrating Leukocytes. *J Immunother Cancer*. 2017;5:18.
31. House IG, Savas P, Lai J, Chen AXY, Oliver AJ, Teo ZL, et al. Macrophage-Derived CXCL9 and CXCL10 Are Required for Antitumor Immune Responses Following Immune Checkpoint Blockade. *Clin Cancer Res*. 2020;26(2):487-504.
32. Italiani P, Boraschi D. From Monocytes to M1/M2 Macrophages: Phenotypical vs. Functional Differentiation. *Front Immunol*. 2014;5:514.
33. Jiang P, Gu S, Pan D, Fu J, Sahu A, Hu X, et al. Signatures of T cell dysfunction and exclusion predict cancer immunotherapy response. *Nat Med*. 2018;24(10):1550-1558.

34. Kantarjian H, Stein A, Gökbuget N, Fielding AK, Schuh AC, Ribera JM, et al. Blinatumomab versus Chemotherapy for Advanced Acute Lymphoblastic Leukemia. N Engl J Med. 2017 Mar 2;376(9):836-847.
35. Ayers M, Lunceford J, Nebozhyn M, Murphy E, Loboda A, Kaufman DR, et al. IFN-γ-related mRNA profile predicts clinical response to PD-1 blockade. *J Clin Invest*. 2017;127(8):2930-2940.
36. Fridman WH, Meylan M, Petitprez F, Sun CM, Italiano A, Sautès-Fridman C. B cells and tertiary lymphoid structures as determinants of tumour immune contexture and clinical outcome. Nat Rev Clin Oncol. 2022 Jul;19(7):441-457.
37. Schumacher TN, Thommen DS. Tertiary lymphoid structures in cancer. Science. 2022 Jan 7;375(6576):eabf9419.
38. Fridman WH, Meylan M, Pupier G, Calvez A, Hernandez I, Sautès-Fridman C. Tertiary lymphoid structures and B cells: An intratumoral immunity cycle. Immunity. 2023 Oct 10;56(10):2254-2269.
39. Gaglia G, Burger ML, Ritch CC, Rammos D, Dai Y, Crossland GE, et al. Lymphocyte networks are dynamic cellular communities in the immunoregulatory landscape of lung adenocarcinoma. Cancer Cell. 2023 May 8;41(5):871-886.e10.
40. Laumont CM, Nelson BH. B cells in the tumor microenvironment: Multi-faceted organizers, regulators, and effectors of anti-tumor immunity. Cancer Cell. 2023 Mar 13;41(3):466-489.
41. Coppola D, Nebozhyn M, Khalil F, Dai H, Yeatman T, Loboda A, et al. Unique ectopic lymph node-like structures present in human primary colorectal carcinoma are identified by immune gene array profiling. Am J Pathol. 2011 Jul;179(1):37-45.
42. Gu-Trantien C, Loi S, Garaud S, Equeter C, Libin M, de Wind A, et al. $CD4^+$ follicular helper T cell infiltration predicts breast cancer survival. J Clin Invest. 2013 Jul;123(7):2873-92.
43. Merritt CR, Ong GT, Church SE, Barker K, Danaher P, Geiss G, et al. Multiplex digital spatial profiling of proteins and RNA in fixed tissue. *Nat Biotechnol*. 2020;38(5):586-599.
44. Danaher P, Kim Y, Nelson B, Griswold M, Yang Z, Piazza E, et al. Advances in mixed cell deconvolution enable quantification of cell types in spatial transcriptomic data. *Nat Commun*. 2022;13(1):385
45. Joshi NS, Akama-Garren EH, Lu Y, Lee D-Y, Chang GP, Li A, et al. Regulatory T Cells in Tumor-Associated Tertiary Lymphoid Structures Suppress Anti-tumor T Cell Responses. *Immunity*. 2015;43(3):579-590.
46. Devi-Marulkar P, Fastenackels S, Karapentiantz P, Goc J, Germain C, Kaplon H, et al. Regulatory T cells infiltrate the tumor-induced tertiary lymphoïd structures and are associated with poor clinical outcome in NSCLC. Commun Biol. 2022 Dec 24;5(1):1416.
47. Schweiger T, Berghoff AS, Glogner C, Glueck O, Rajky O, Traxler Det al. Tumor-infiltrating lymphocyte subsets and tertiary lymphoid structures in pulmonary metastases from colorectal cancer. Clin Exp Metastasis. 2016 Oct;33(7):727-39.
48. Cottrell TR, Thompson ED, Forde PM, Stein JE, Duffield AS, Anagnostou V, et al. Pathologic features of response to neoadjuvant anti-PD-1 in resected non-small-cell lung carcinoma: a proposal for quantitative immune-related pathologic response criteria (irPRC). Ann Oncol. 2018 Aug 1;29(8):1853-1860.

49. van Dijk N, Gil-Jimenez A, Silina K, Hendricksen K, Smit LA, de Feijter JM, et al. Preoperative ipilimumab plus nivolumab in locoregionally advanced urothelial cancer: the NABUCCO trial. Nat Med. 2020 Dec;26(12):1839-1844.
50. Davids MS, Kim HT, Bachireddy P, Costello C, Liguori R, Savell A, et al. Ipilimumab for Patients with Relapse after Allogeneic Transplantation. N Engl J Med. 2016 Jul 14;375(2):143-53.
51. Penter L, Zhang Y, Savell A, Huang T, Cieri N, Thrash EM, et al. Molecular and cellular features of CTLA-4 blockade for relapsed myeloid malignancies after transplantation. Blood. 2021 Jun 10;137(23):3212-3217.
52. Garcia JS, Flamand Y, Penter L, Keng M, Tomlinson BK, Mendez LM, et al. Ipilimumab plus decitabine for patients with MDS or AML in posttransplant or transplant-naïve settings. Blood. 2023 Apr 13;141(15):1884-1888.
53. Mellman I, Chen DS, Powles T, Turley SJ. The cancer-immunity cycle: Indication, genotype, and immunotype. Immunity. 2023 Oct 10;56(10):2188-2205.
54. Bailur JK, McCachren SS, Pendleton K, Vasquez JC, Seo Lim H, Duffy A, et al. Risk-associated alterations in marrow T cells in pediatric leukemia. *JCI Insight*. 2020;5(16):e140179.
55. Koedijk JB, van der Werf I, Calkoen FG, Nierkens S, Kaspers GJL, Zwaan CM, et al. Paving the Way for Immunotherapy in Pediatric Acute Myeloid Leukemia: Current Knowledge and the Way Forward. *Cancers (Basel)*. 2021;13(17):4364.
56. Duan Q, Zhang H, Zheng J, Zhang L. Turning Cold into Hot: Firing up the Tumor Microenvironment. Trends Cancer. 2020 Jul;6(7):605-618.
57. Brauneck F, Fischer B, Witt M, Muschhammer J, Oelrich J, Henrique da Costa Avelar P, et al. TIGIT blockade repolarizes AML-associated TIGIT$^+$ M2 macrophages to an M1 phenotype and increases CD47-mediated phagocytosis. *J Immunother Cancer*. 2022;10(12):e004794.
58. Chen JH, Nieman LT, Spurrell M, Jorgji V, Richieri P, Xu KH et al. Spatial analysis of human lung cancer reveals organized immune hubs enriched for stem-like CD8 T cells and associated with immunotherapy response. *bioRxiv* 2023.
59. Jansen CS, Prokhnevska N, Master VA, Sanda MG, Carlisle JW, Bilen MA, et al. An intra-tumoral niche maintains and differentiates stem-like CD8 T cells. Nature. 2019 Dec;576(7787):465-470.
60. Kriner MA, van Raay K, Reeves JW, Fuhrman KA, Klock A, Kutchma A, et al. Spatially resolved T-cell receptor profiling elucidates relationships between TCR diversity, immune-infiltration, and cancer-associated pathways. Cancer Res 2022;82(12_Suppl):Abstract nr 1364.
61. Hudson WH, Sudmeier LJ. Localization of T cell clonotypes using the Visium spatial transcriptomics platform. STAR Protoc. 2022 Jun 10;3(2):101391.
62. He S, Bhatt R, Brown C, Brown EA, Buhr DL, Chantranuvatana K, et al. High-plex imaging of RNA and proteins at subcellular resolution in fixed tissue by spatial molecular imaging. Nat Biotechnol. 2022 Dec;40(12):1794-1806.
63. Janesick A, Shelansky R, Gottscho AD, Wagner F, Roualt M, Beliakoff G, et al. High resolution mapping of the breast cancer tumor microenvironment using integrated single cell, spatial and in situ analysis of FFPE tissue. *bioRxiv* 2022.
64. Casparie M, Tiebosch AT, Burger G, Blauwgeers H, van de Pol A, van Krieken JHJM, et al. Pathology databanking and biobanking in The Netherlands, a central role for PALGA, the nationwide histopathology and cytopathology data network and archive. *Cell Oncol*. 2007;29(1):19-24.

65. Bankhead P, Loughrey MB, Fernández JA, Dombrowski Y, McArt DG, Dunne PD, et al. QuPath: Open source software for digital pathology image analysis. *Sci Rep*. 2017;7(1):16878.
66. Schmidt U, Weigert M, Broaddus C, Myers G. Cell detection with star-convex polygons. *International Conference on Medical Image Computing and Computer-Assisted Intervention*. 2018;265-273.
67. Delaunay B. Sur la sphère vide. *Bull. Acad. Sci. URSS*. 1934:793–800.
68. Ge SX, Son EW, Yao R. iDEP: an integrated web application for differential expression and pathway analysis of RNA-Seq data. *BMC Bioinformatics*. 2018;19(1):534.
69. Ashburner M, Ball CA, Blake JA, Botstein D, Butler H, Cherry JM, et al. Gene ontology: tool for the unification of biology. The Gene Ontology Consortium. *Nat Genet*. 2000;25(1):25-29.
70. Gene Ontology Consortium. The Gene Ontology resource: enriching a GOld mine. *Nucleic Acids Res*. 2021;49(D1):D325-D334.
71. Martens M, Ammar A, Riutta A, Waagmeester A, Slenter DN, Hanspers K, et al. WikiPathways: connecting communities. Nucleic Acids Res. 2021 Jan 8;49(D1):D613-D621.
72. Beyer M, Mallmann MR, Xue J, Staratcheck-Jox A, Vorholt D, Krebs W, et al. High-resolution transcriptome of human macrophages. *PLoS One*. 2012;7(9):e45466.
73. Zhang Y, Parmigiani G, Johnson WE. *ComBat-seq*: batch effect adjustment for RNA-seq count data. NAR Genom Bioinform. 2020 Sep;2(3):lqaa078.
74. Cerami E, Gao J, Dogrusoz U, Gross BE, Sumer SO, Aksoy BA, et al. The cBio cancer genomics portal: an open platform for exploring multidimensional cancer genomics data. Cancer Discov. 2012 May;2(5):401-4.

Table Legends

Supplementary Table 1. Clinical characteristics of the primary study cohort, supplemented with information on immune-infiltration, performed assays, and T cell networks.

Supplementary Table 2. List of differentially expressed genes between immune-infiltrated and immune-depleted pediatric AML in the TARGET-AML cohort.

Supplementary Table 3. List of significantly up- or downregulated pathways comparing immune-infiltrated versus immune-depleted cases using ssGSEA.

Supplementary Table 4. Clinical characteristics of the adult AML cohort treated with ipilimumab-based therapy.

Supplementary Table 5. Target antigens, antibody clones and suppliers of antibodies used for pediatric AML bone marrow IHC.

Supplementary Table 6. Target antigens, antibody clones, suppliers, dilution of markers, diluents, and antigen retrieval conditions used for adult AML bone marrow immunofluorescence.

Figure Legends

Figure 1. Characterizing T cell infiltration in pediatric AML cases and non-leukemic controls.

(A) Schematic overview of the study population, used techniques, and the digital image analysis pipeline. AML cases are categorized in immune-infiltrated (red) and immune-depleted (blue) groups according to their T cell infiltration levels (>median of non-leukemic controls). (B-C) Representative bone marrow biopsy images from a treatment-naïve pediatric AML case (B) and a non-leukemic control (C) showing H&E staining, $CD3^+$ T cells, and $CD8^+$ T cells. White lobules indicate adipocytes. (D-E) Comparison of the normalized abundance of $CD3^+$ T cells (D) and $CD8^+$ T cells (E) in the BM between pediatric AML cases and non-leukemic controls using the Mann-Whitney test. The dashed lines indicate the median $CD3^+$ (D) and $CD8^+$ (E) T cell abundance of non-leukemic controls, respectively. (F-G) Normalized abundance of $CD3^+$ (F) and $CD8^+$ T cells (G) per cytogenetic subgroup (Kruskal-Wallis followed by Dunn's multiple comparison test). 'Normal' indicates normal karyotype, while 'Others' is a merge of cytogenetic abnormalities different from the five defined cytogenetic subgroups. See Table S1. 'Complex' indicates cases with complex karyotype AML (≥3 chromosomal abnormalities). The dashed lines shown in Figure 1D-E are also shown in Figure 1F-G. (H-I) Estimated abundance of T- (H) and $CD8^+$ T (I) cells in the bone marrow of treatment-naïve pediatric AML cases in the TARGET-AML cohort (Kruskal-Wallis followed by Dunn's multiple comparison test).

Figure 2. Transcriptional differences between immune-infiltrated and immune-depleted pediatric AML.

(A) Comparison of the normalized abundance of $CD20^+$ B cells in the bone marrow of pediatric AML (CD20-staining available for 69 cases) with $CD3^+$ T cell levels above or below the median of non-leukemic controls (referred to as immune-infiltrated and immune-depleted, respectively; Mann-Whitney test). (B) Overall survival between immune-infiltrated and immune-depleted complex karyotype pediatric AML cases in the TARGET-AML cohort. (C) Volcano plot of differentially expressed genes between immune-infiltrated (n=6) and immune-depleted (n=17) pediatric AML BM biopsies, identified using *DEseq2* with an FDR cut-off of 0.05 and minimum fold change (FC) of 2. (D) Single-sample gene set enrichment analysis of differentially expressed genes between immune-infiltrated and immune-depleted cases using the GO Biological Processes gene set with an FDR cut-off of 0.05. WikiPathways-related results are shown in Table S3. (E) Correlation plot of the negative correlation between the M2-predominance score and the normalized number of $CD3^+$ T cells, calculated using Spearman correlation. (F) Comparison of the M2-predominance score

between immune-infiltrated (n=6) and immune-depleted (n=17) cases using the Mann-Whitney test. (G) Correlation plot of the negative correlation between the M2-predominance score and the estimated abundance of T cells in the bone marrow of TARGET-AML cases, calculated using Spearman correlation. (H) Comparison of the M2-predominance score between immune-infiltrated (n=80) and immune-depleted (n=79) cases using the Mann-Whitney test. (I) Comparison of the M2-predominance score between relapsed or refractory adult AML with anti-leukemic activity (ALA) or non-response (NR) to flotetuzumab, evaluated using the Mann-Whitney test. (J) Area under the receiver operating characteristic curves measuring the predictive ability of the M2-predominance score (black), T cell inflamed gene expression profile (GEP; light blue), CD8 score (grey), IFN-*γ* score (pink*),* and the tumor immune dysfunction and exclusion score (TIDE; orange*)* relapsed or refractory adult AML for response to flotetuzumab.

Figure 3. Spatially organized T cell networks in the bone marrow of pediatric AML.

(A) Illustration of the identification of directly interacting T cells (above) and T cell networks (below) using Delaunay Triangulation. (B) Comparison of the normalized abundance of T cell networks between immune-infiltrated (n=22), immune-depleted (n=50), and non-leukemic control biopsies (n=10; Kruskal-Wallis followed by Dunn's multiple comparisons test). (C) Correlation plot of the positive correlation between the normalized number of $CD3^+$ T cells and the normalized number of T cell networks in both AML and non-leukemic control biopsies (n=82), calculated using Spearman correlation. (D) Comparison of the number of T cell networks with at least 100 T cells/network between immune-infiltrated (n=22), immune-depleted (n=50), and non-leukemic control biopsies (n=10; Kruskal-Wallis followed by Dunn's multiple comparisons test). (E-G) Representative images of large T cell networks in three immune-infiltrated pediatric AML cases. (H-I) Representative images of large T cell networks (H) that colocalize with dense networks of $CD20^+$ B cells (I).

Figure 4. Composition of tertiary lymphoid structure-like aggregates in immune-infiltrated pediatric AML.

(A-C) Overview of the different types of regions profiled using spatial transcriptomics in immune-infiltrated biopsies with immune aggregates (A), immune-infiltrated biopsies without immune-aggregates (B), and non-leukemic biopsies (C). Green cells indicate T cells, blue cells indicate B cells, and pink/purple cells indicate AML blasts. These examples do not necessarily reflect the actual abundance of these subsets. (D) UMAP of transcriptomic profiles of various region types, organized into two separate clusters. (E-G) Comparison of the expression of the '12chem' (E), 'Tfh' (F), and 'TLS imprint' (G) signatures across different region types (Kruskal-Wallis followed by Dunn's multiple comparisons test). (H-L)

Deconvoluted abundance of various cell subsets and the M2-predominance score compared across different region types (Kruskal-Wallis followed by Dunn's multiple comparisons test).

Figure 5. Spatially organized immune aggregates in the bone marrow and at extramedullary sites of adult AML treated with ipilimumab-based treatment.

(A) Schematic overview of adult AML cases that were treated according to either of two clinical trials, the used techniques, and the examined variables. (B-G) Longitudinal overview of (large) T cell networks and AML blasts in bone marrow biopsies before (baseline) or after treatment (EC=end of course; EOT=end of treatment). Green IDs indicate responders, purple IDs indicate non-responders. AML 1006 was the exceptional responder with >4.8 years of sustained remission. The AML blast percentage was the average of the percentages in the aspirate and the core biopsy. CR=complete remission. (H) Comparison of the normalized density of $CD20^+$ B cells inside large T cell networks and in the total biopsy areas (Wilcoxon matched-pairs signed rank test). (I-J) Representative multiplex immunofluorescence images of large T cell networks with an enrichment of B cells.

Supplementary Figure 1. AML blasts and differentiation stage in relation to T- and $CD8^+$ T cell infiltration in the bone marrow.

(A-B) Correlation plot between the normalized number of $CD3^+$ (A) and $CD8^+$ (B) T cells and leukemic blasts in the bone marrow (blast % available for 65 cases), calculated using Spearman correlation. (C-D) Comparison of the normalized abundance of $CD3^+$ (C) and $CD8^+$ (D) T cells in the bone marrow across AML differentiation stages (FAB-classifications; Kruskal-Wallis followed by Dunn's multiple comparisons test). Data are presented as mean plus range. (E-F) Comparison of the estimated abundance of T (E) and $CD8^+$ (F) T cells in the bone marrow of TARGET-AML cases across AML differentiation stages (FAB-classifications; Kruskal-Wallis followed by Dunn's multiple comparisons test). Data are presented as mean plus range. (G-H) Correlation plot between the estimated number of T (G) and $CD8^+$ (H) T cells and leukemic blasts in the bone marrow (blast % available for 154 cases) of TARGET-AML cases, calculated using Spearman correlation.

Supplementary Figure 2. Overall survival, M2-like macrophage abundance, and differentially expressed genes in immune-infiltrated and immune-depleted cases across two cohorts.

(A-B) Overall survival between immune-infiltrated and immune-depleted pediatric AML cases in our cohort (A) and in the TARGET-AML cohort (B). (C) Volcano plot of differentially expressed genes between immune-infiltrated and immune-depleted cases in the TARGET-AML cohort, identified using *DEseq2* with an FDR cut-off of 0.05 and minimum fold change

(FC) of 2. (D-E) Correlation plots of the correlation between the M2-predominance score and the normalized (D; our cohort) or estimated (E; TARGET-AML cohort) abundance of $CD8^+$ T cells, calculated using Spearman correlation.

Supplementary Figure 3. Representative images of bone marrow biopsies of immune-infiltrated and immune-depleted pediatric AML, and a non-leukemic control.

(A-B) Representative images of $CD3^+$ T cells in the bone marrow of immune-depleted cases. (C-D) Representative images of large T cell networks (C) that colocalize with a dense network of B cells (D). (E) Representative image of $CD3^+$ T cell infiltration in the bone marrow of a non-leukemic control.

Supplementary Figure 4. Composition of tertiary lymphoid structure-like aggregates in immune-infiltrated pediatric AML. (A-L) Deconvoluted, absolute or relative abundance of various cell subsets across several region types (Kruskal-Wallis followed by Dunn's multiple comparisons test).

Supplementary Figure 5. Large T cell networks in post-treatment bone marrow and extramedullary biopsies of adult AML treated with ipilimumab-based treatment.

(A-B) Representative images of large T cell networks with no or hardly any B cells in bone marrow biopsies of ipilimumab-treated adult AML cases. (C) Comparison of the B cell density in large T cell networks between pre- and post-treatment bone marrow biopsies. Every dot reflects a large T cell network. Examined using the Mann-Whitney test (D) Overview of large T cell networks in extramedullary pre- and post-treatment biopsies (unpaired t test). (E-F) representative images of extramedullary pre- and post-treatment biopsies.

Figure 1

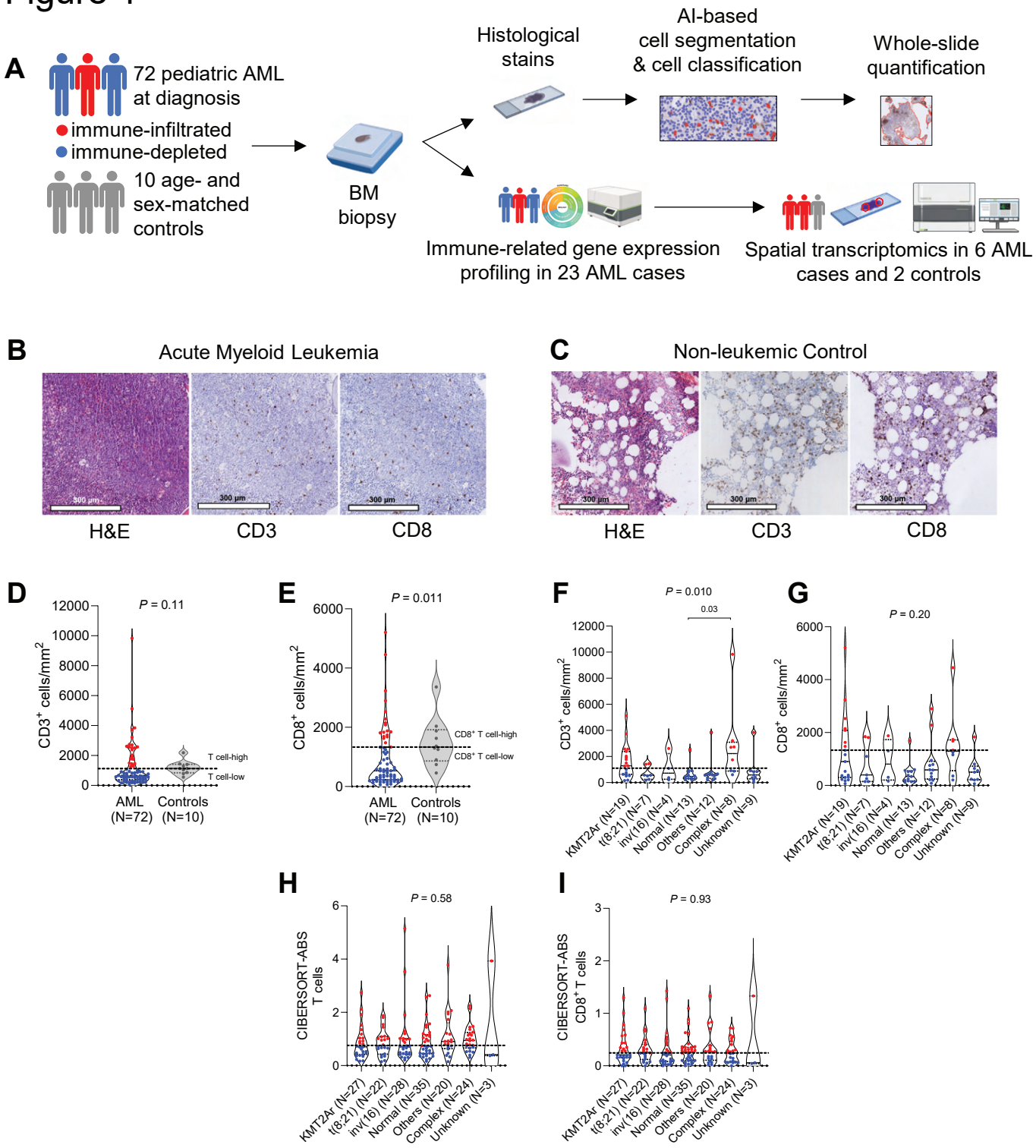
A
72 pediatric AML at diagnosis
immune-infiltrated
immune-depleted
10 age- and sex-matched controls
BM biopsy
Histological stains
AI-based cell segmentation & cell classification
Whole-slide quantification
Immune-related gene expression profiling in 23 AML cases
Spatial transcriptomics in 6 AML cases and 2 controls
B
Acute Myeloid Leukemia
H&E
CD3
CD8
C
Non-leukemic Control
H&E
CD3
CD8
D
P = 0.11
CD3+ cells/mm2
T cell-high
T cell-low
AML (N=72)
Controls (N=10)
E
P = 0.011
CD8+ cells/mm2
CD8+ T cell-high
CD8+ T cell-low
AML (N=72)
Controls (N=10)
F
P = 0.010
0.03
CD3+ cells/mm2
KMT2Ar (N=19)
t(8;21) (N=7)
inv(16) (N=4)
Normal (N=13)
Others (N=12)
Complex (N=8)
Unknown (N=9)
G
P = 0.20
CD8+ cells/mm2
KMT2Ar (N=19)
t(8;21) (N=7)
inv(16) (N=4)
Normal (N=13)
Others (N=12)
Complex (N=8)
Unknown (N=9)
H
P = 0.58
CIBERSORT-ABS T cells
KMT2Ar (N=27)
t(8;21) (N=22)
inv(16) (N=28)
Normal (N=35)
Others (N=20)
Complex (N=24)
Unknown (N=3)
I
P = 0.93
CIBERSORT-ABS CD8+ T cells
KMT2Ar (N=27)
t(8;21) (N=22)
inv(16) (N=28)
Normal (N=35)
Others (N=20)
Complex (N=24)
Unknown (N=3)

Figure 2

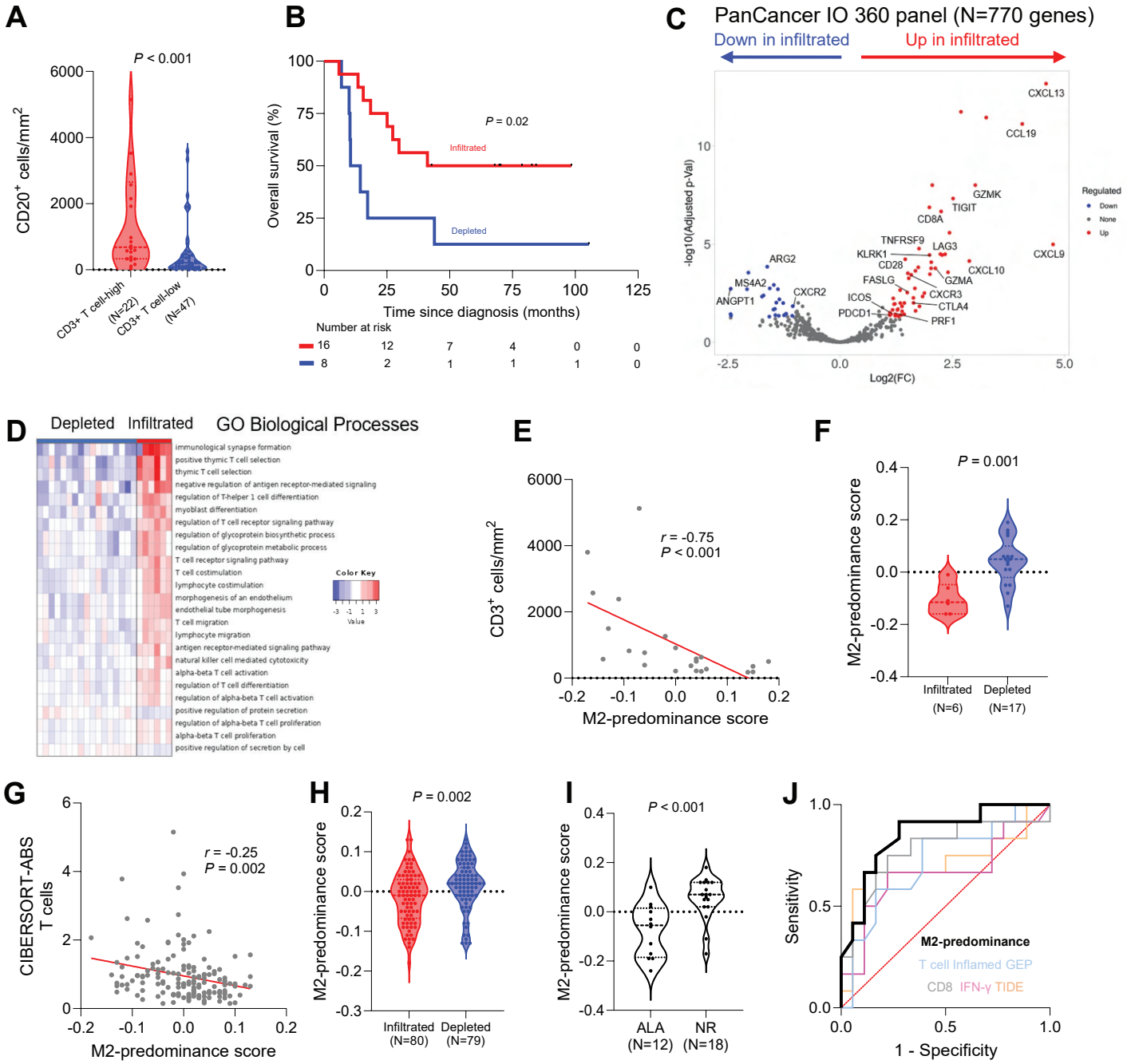
A
P < 0.001
CD20+ cells/mm2
6000
4000
2000
0
CD3+ T cell-high (N=22)
CD3+ T cell-low (N=47)
B
Overall survival (%)
100
75
50
25
0
P = 0.02
Infiltrated
Depleted
0
25
50
75
100
125
Time since diagnosis (months)
Number at risk
16 12 7 4 0 0
8 2 1 1 1 0
C
PanCancer IO 360 panel (N=770 genes)
Down in infiltrated
Up in infiltrated
-log10(Adjusted p-Val)
Log2(FC)
CXCL13
CCL19
GZMK
TIGIT
CD8A
TNFRSF9
LAG3
KLRK1
CD28
CXCL10
CXCL9
GZMA
FASLG
CXCR3
ICOS
CTLA4
PDCD1
PRF1
ARG2
MS4A2
ANGPT1
CXCR2
Regulated
Down
None
Up
D
Depleted
Infiltrated
GO Biological Processes
immunological synapse formation
positive thymic T cell selection
thymic T cell selection
negative regulation of antigen receptor-mediated signaling
regulation of T-helper 1 cell differentiation
myoblast differentiation
regulation of T cell receptor signaling pathway
regulation of glycoprotein biosynthetic process
regulation of glycoprotein metabolic process
T cell receptor signaling pathway
T cell costimulation
lymphocyte costimulation
morphogenesis of an endothelium
endothelial tube morphogenesis
T cell migration
lymphocyte migration
antigen receptor-mediated signaling pathway
natural killer cell mediated cytotoxicity
alpha-beta T cell activation
regulation of T cell differentiation
regulation of alpha-beta T cell activation
positive regulation of protein secretion
regulation of alpha-beta T cell proliferation
alpha-beta T cell proliferation
positive regulation of secretion by cell
Color Key
Value
E
CD3+ cells/mm2
6000
4000
2000
0
r = -0.75
P < 0.001
-0.2
-0.1
0.0
0.1
0.2
M2-predominance score
F
M2-predominance score
P = 0.001
0.4
0.2
0.0
-0.2
-0.4
Infiltrated (N=6)
Depleted (N=17)
G
CIBERSORT-ABS T cells
6
4
2
0
r = -0.25
P = 0.002
-0.2
-0.1
0.0
0.1
0.2
M2-predominance score
H
M2-predominance score
P = 0.002
0.2
0.1
0.0
-0.1
-0.2
-0.3
Infiltrated (N=80)
Depleted (N=79)
I
M2-predominance score
P < 0.001
0.4
0.2
0.0
-0.2
-0.4
ALA (N=12)
NR (N=18)
J
Sensitivity
1.0
0.5
0.0
M2-predominance
T cell Inflamed GEP
CD8
IFN-γ TIDE
0.0
0.5
1.0
1 - Specificity

Figure 3

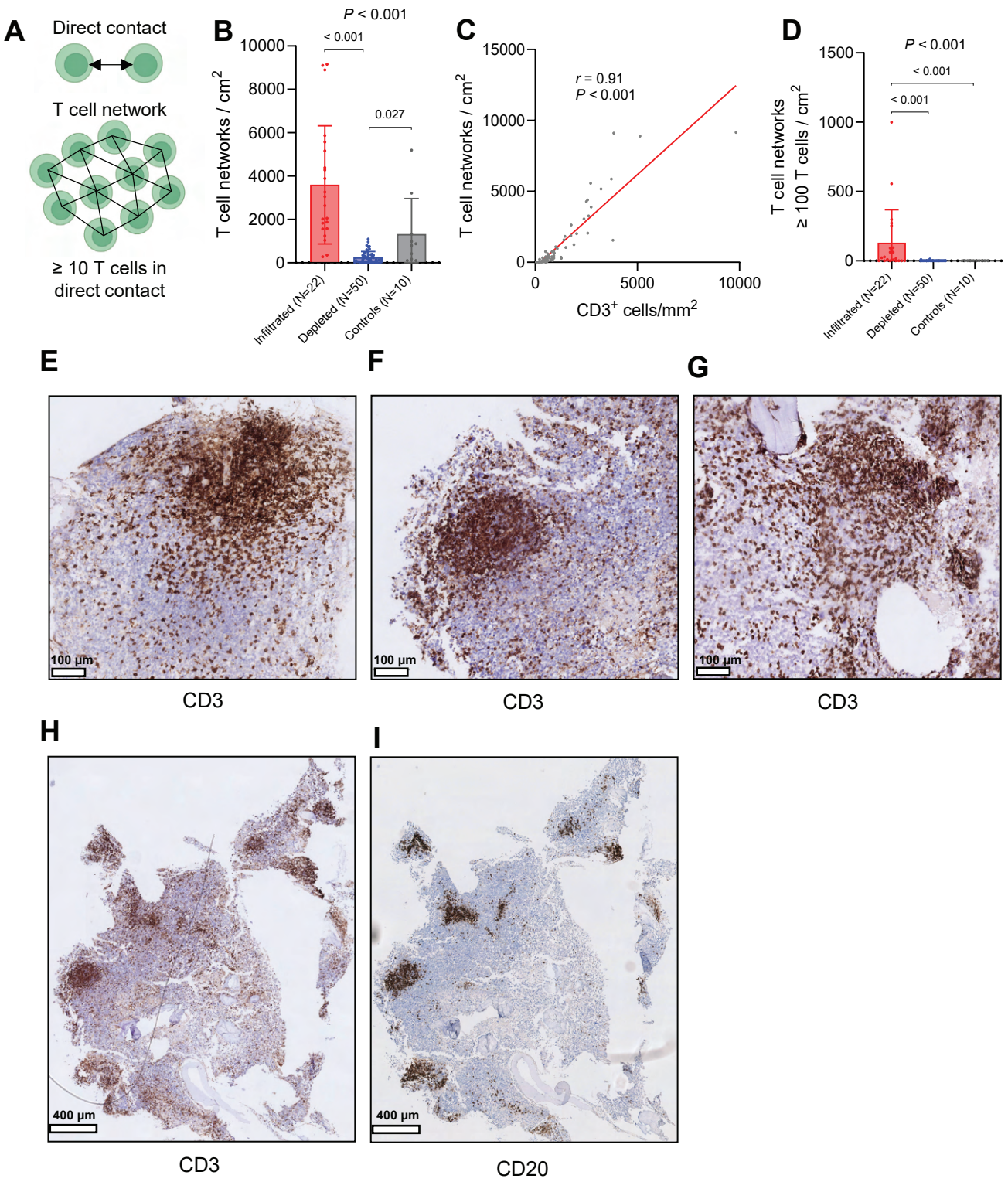
A
Direct contact
T cell network
≥ 10 T cells in direct contact
B
P < 0.001
< 0.001
0.027
T cell networks / cm2
10000
8000
6000
4000
2000
0
Infiltrated (N=22)
Depleted (N=50)
Controls (N=10)
C
r = 0.91
P < 0.001
T cell networks / cm2
15000
10000
5000
0
5000
10000
CD3+ cells/mm2
D
P < 0.001
< 0.001
< 0.001
T cell networks ≥ 100 T cells / cm2
1500
1000
500
0
Infiltrated (N=22)
Depleted (N=50)
Controls (N=10)
E
100 µm
CD3
F
100 µm
CD3
G
100 µm
CD3
H
400 µm
CD3
I
400 µm
CD20

Figure 4

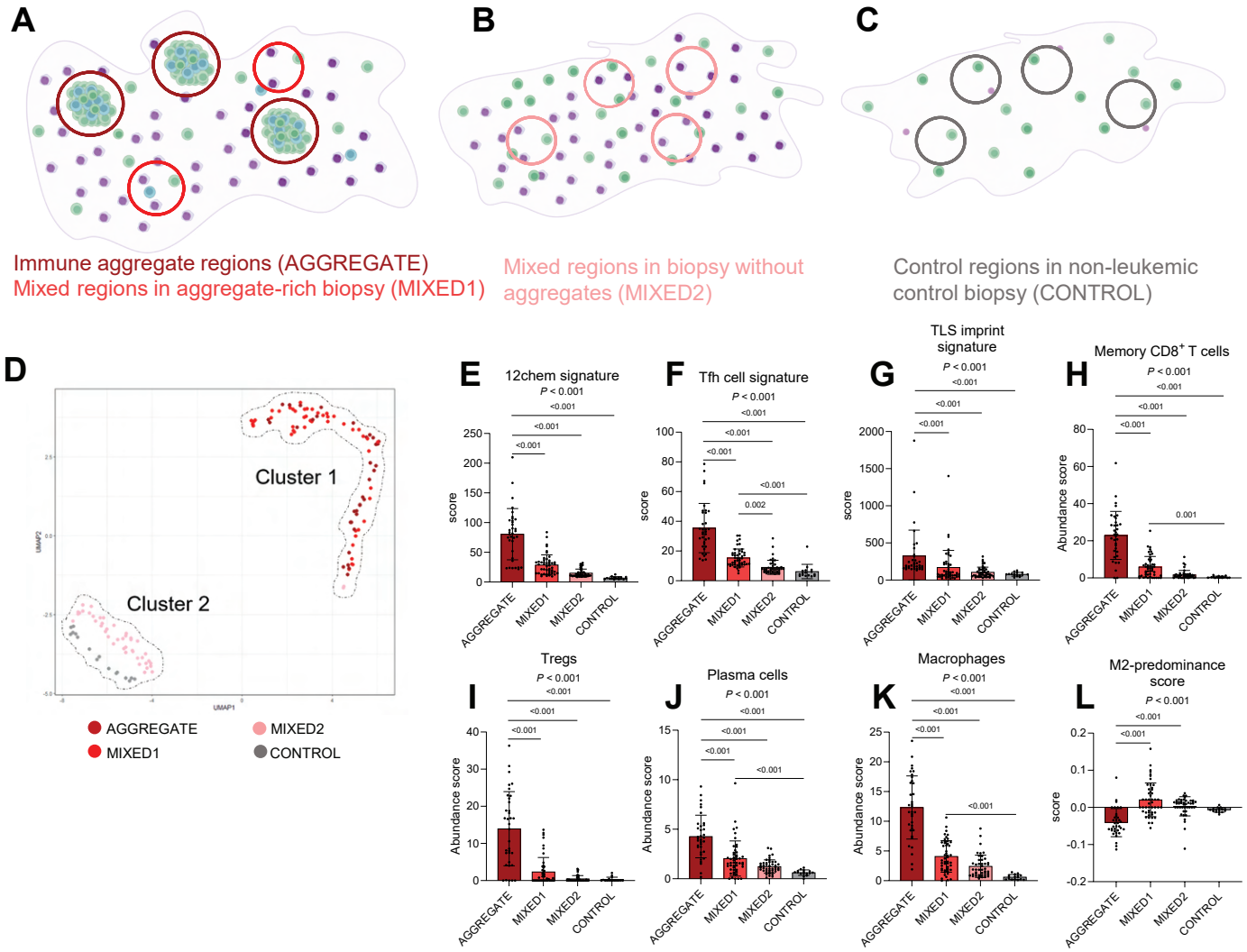
A
B
C
Immune aggregate regions (AGGREGATE)
Mixed regions in aggregate-rich biopsy (MIXED1)
Mixed regions in biopsy without aggregates (MIXED2)
Control regions in non-leukemic control biopsy (CONTROL)
D
Cluster 1
Cluster 2
UMAP1
UMAP2
AGGREGATE
MIXED1
MIXED2
CONTROL
E
12chem signature
F
Tfh cell signature
G
TLS imprint signature
H
Memory CD8+ T cells
I
Tregs
J
Plasma cells
K
Macrophages
L
M2-predominance score
P < 0.001
score
Abundance score
AGGREGATE
MIXED1
MIXED2
CONTROL

Figure 5

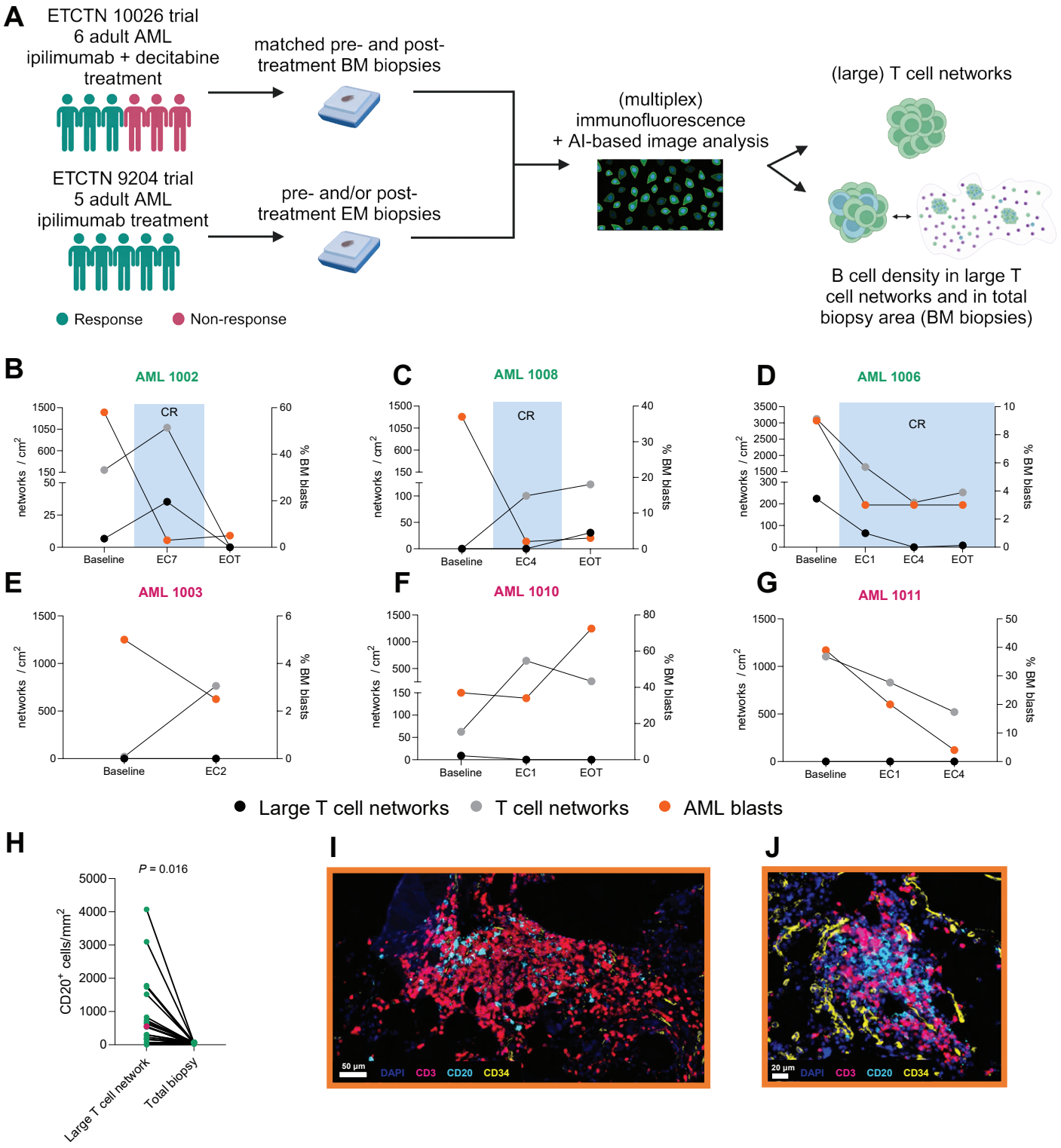
A
ETCTN 10026 trial
6 adult AML
ipilimumab + decitabine
treatment
matched pre- and post-
treatment BM biopsies
ETCTN 9204 trial
5 adult AML
ipilimumab treatment
pre- and/or post-
treatment EM biopsies
(multiplex)
immunofluorescence
+ AI-based image analysis
(large) T cell networks
B cell density in large T
cell networks and in total
biopsy area (BM biopsies)
Response
Non-response
B
AML 1002
C
AML 1008
D
AML 1006
E
AML 1003
F
AML 1010
G
AML 1011
CR
networks / cm2
% BM blasts
Baseline
EC7
EOT
EC4
EC1
EC2
Large T cell networks
T cell networks
AML blasts
H
P = 0.016
CD20+ cells/mm2
Large T cell network
Total biopsy
I
50 µm
DAPI
CD3
CD20
CD34
J
20 µm
DAPI
CD3
CD20
CD34

Supplementary Figure 1

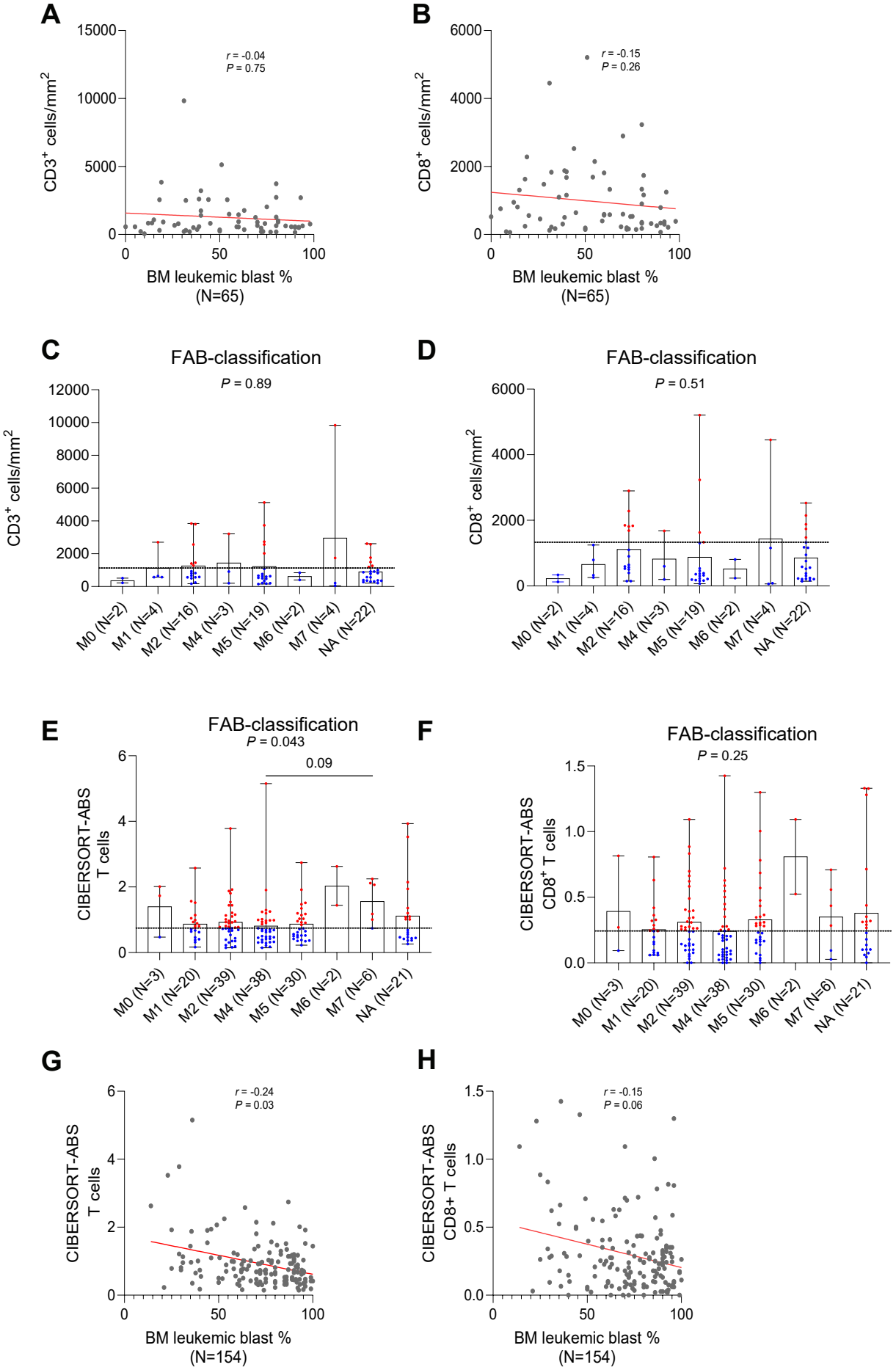

Supplementary Figure 2

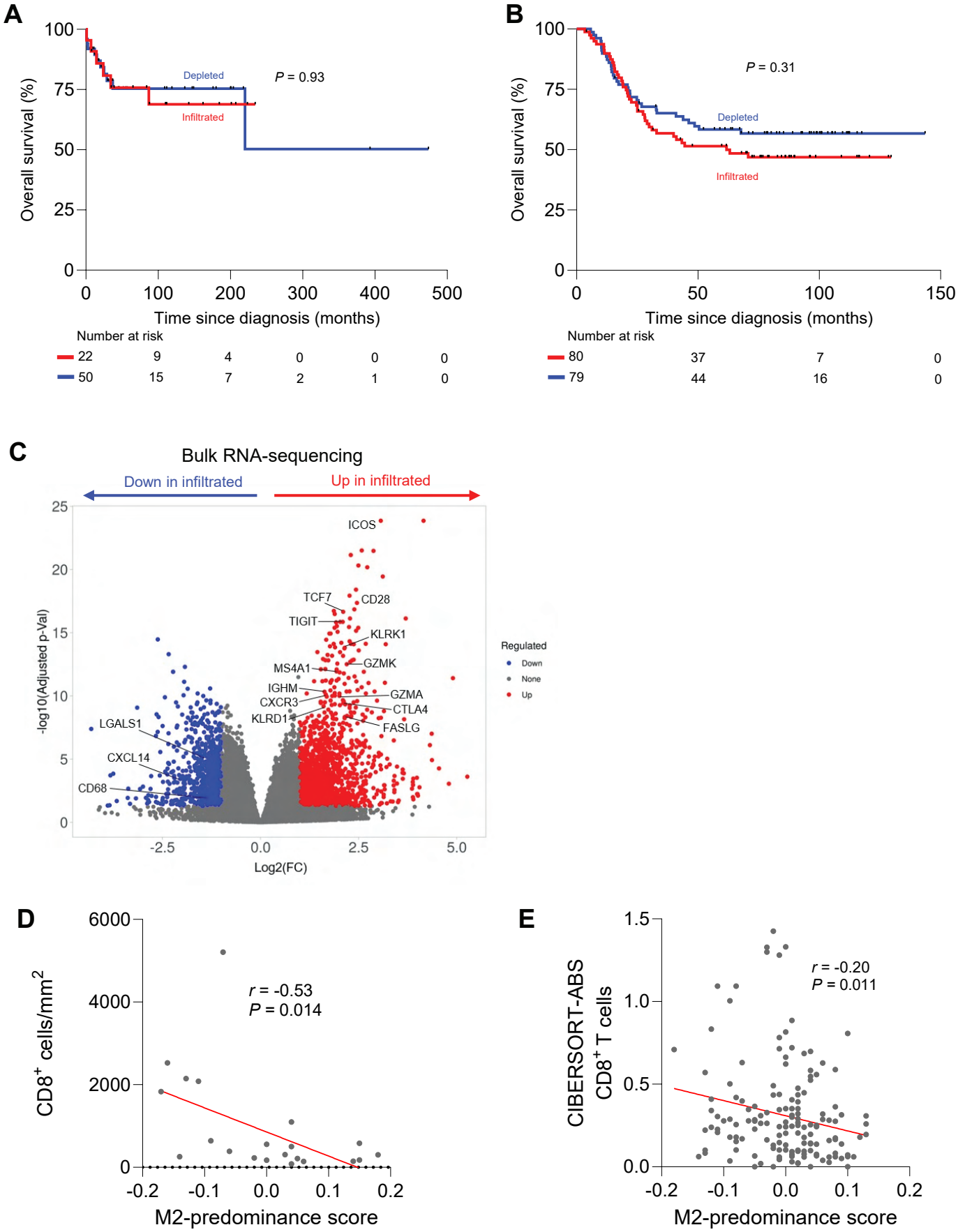

Supplementary Figure 3

A

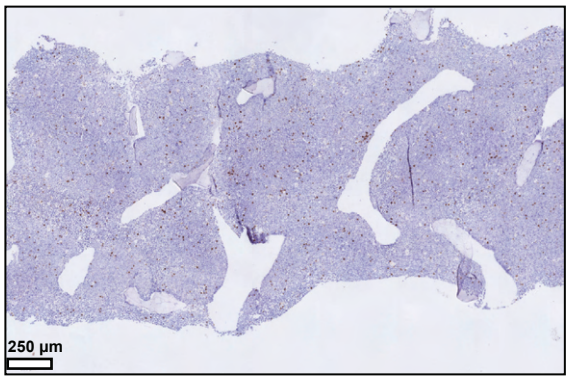

CD3

B

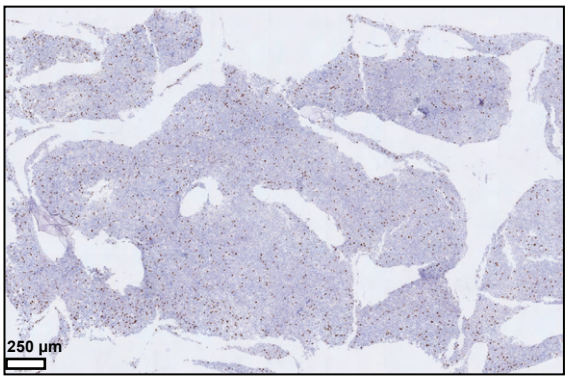

CD3

C

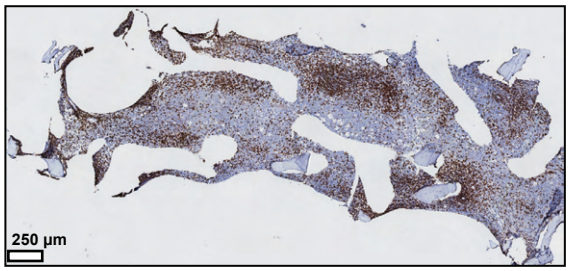

CD3

D

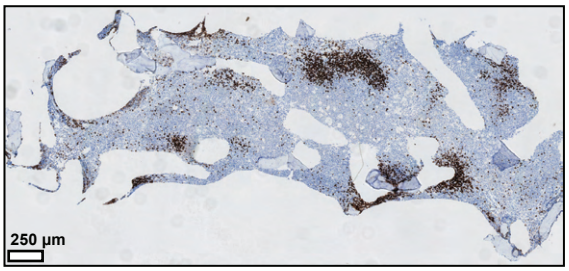

CD20

E

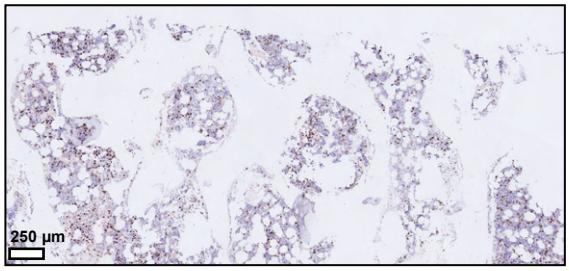

CD3

Supplementary Figure 4

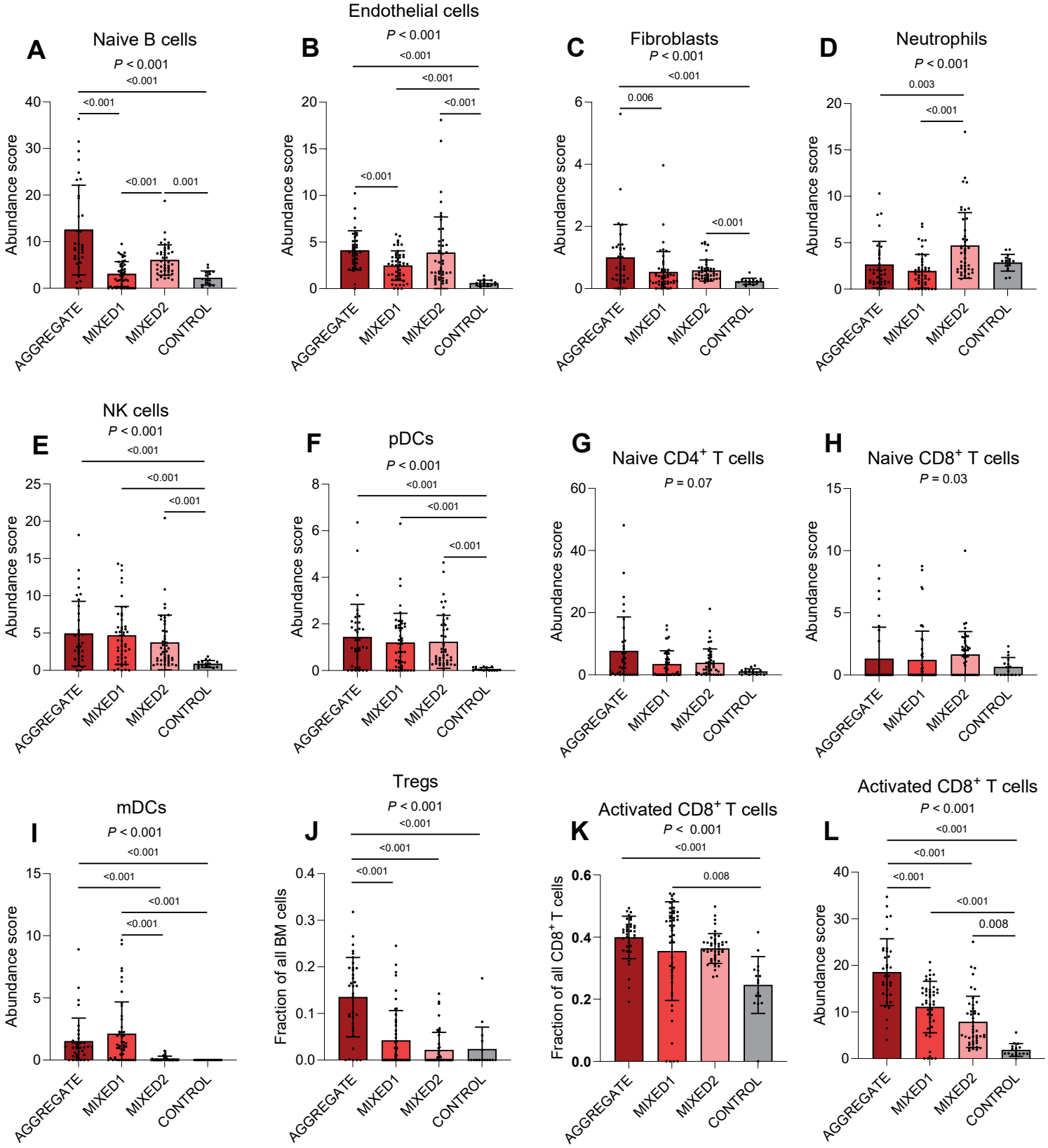
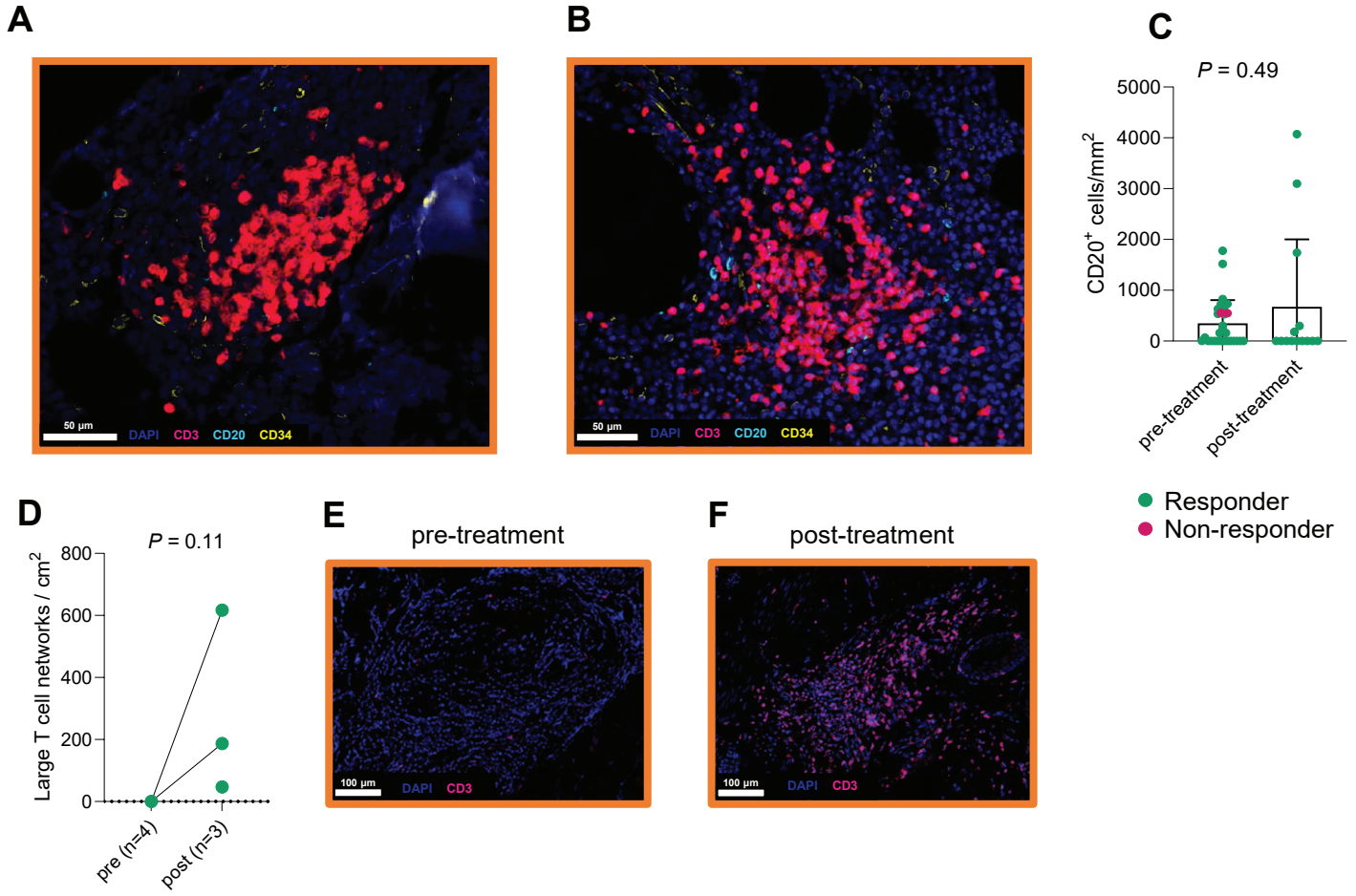
Supplementary Figure 5